Optimization and Computational Fluid Dynamics (CFD) Analysis of a Novel Left Ventricular Assist Device (LVAD) Configuration

Yinan Bao

M.Sc. in Mechanical Engineering

Department of Mechanical Engineering

McGill University

Montreal, Quebec

December 2021

A thesis submitted to McGill University in partial fulfillment of the requirements of the degree of

Master of Science

ABSTRACT

Although the gold standard for treating end-stage heart failure (Class III and Class IV) is heart transplant, implantation of Left Ventricular Assist Devices (LVADs) as an alternative treatment has been widely used due to limited availability of donor hearts. Despite the great improvement in expectancy and quality of life for patients treated with LVADs, the postoperative complications including bleeding, hemolysis and thrombosis still exist, making patients suffer. Many studies have shown that these complications are highly related to the implementation of LVADs since continuous exposure of blood to the devices causes the accumulated damage to blood cells.

The main objective of this thesis is to generate numerical simulations to verify the concept of a novel design of axial-flow LVAD and optimize its geometry in order to increase its hydraulic efficiency and minimize blood damage. Unlike conventional axial-flow LVADs, the blades of the novel design are mounted on the shroud of the device. Hubless LVAD could significantly reduce the operating speed of the device while capable of providing necessary blood flow due to larger pumping volume per unit time. In addition, a secondary diffuser was implemented to guide the flow and increase its hydraulic efficiency. The geometry was built using software CAESES and then parameterized and exported into ANSYS for meshing and further simulation. Multiple evaluation parameters were monitored and imported into CAESES as objectives to run the design explorations by varying the design variables and achieve optimal configuration. Comparing the baseline model, the optimized geometry increased its pressure rise between outlet and inlet from 2806 Pa to 14102 Pa while the hemolysis index only increased approximately 15%, from 0.0021% to 0.0024%. The hydraulic efficiency also increased from 7.6% to 59.6%.

RÉSUMÉ

Bien que la référence pour le traitement de l'insuffisance cardiaque terminale (classe III et classe IV) soit la transplantation cardiaque, l'implantation de dispositifs d'assistance ventriculaire gauche (LVADs en anglais) comme traitement alternatif a été largement utilisée en raison de la disponibilité limitée de cœurs de donneurs. Malgré les progrès considérables réalisés dans ce domaine de l'espérance et de la qualité de vie des patients traités par LVAD, les complications postopératoires telles que saignements, hémolyse et thrombose existent toujours, faisant souffrir les patients. De nombreuses études ont montré que ces complications sont fortement liées à la mise en œuvre des LVAD puisque l'exposition continue du sang aux dispositifs provoque les dommages accumulés aux cellules sanguines.

L'objectif principal de cette thèse est de générer des simulations numériques pour vérifier le concept d'une nouvelle conception de LVAD à écoulement axial et optimiser sa géométrie afin d'augmenter son efficacité hydraulique et de minimizer les dommages au sang. Contrairement aux LVAD à flux axial conventionnel, les lames de la nouvelle conception sont montées sur le carénage du dispositif. Le LVAD sans moyeu pourrait réduire considérablement la vitesse de fonctionnement de l'appareil tout en étant capable de fournir le flux sanguin nécessaire en raison d'un volume de pompage plus important par unité de temps. De plus, un diffuseur secondaire a été mis en place pour guider le débit et augmenter son efficacité hydraulique. La géométrie a été construite à l'aide du logiciel CAESES, puis paramétrée et exportée dans ANSYS pour le maillage et la simulation ultérieure. De multiples paramètres d'évaluation ont été surveillés et importés dans CAESES en tant qu'objectifs pour exécuter les explorations de conception en faisant varier les variables de conception et obtenir une configuration optimale. En comparant le modèle de base, la géométrie optimisée a augmenté son élévation de pression entre la sortie et l'entrée de 2806 Pa à 14102 Pa tandis que l'indice d'hémolyse n'a augmenté que d'environ 15%, passant de 0.0021% à 0.0024%. Le rendement hydraulique a également augmenté de 7.6 % à 59.6 %.

ACKNOWLEDGEMENTS

I would like to first acknowledge my two supervisors, Prof. Rosaire Mongrain and Dr. Renzo Cecere, for your great guidance and academic advice during the whole period of the project. You taught me more than how to solve a practical problem but more importantly, how to think and learn as a real researcher instead of a student. Thank you so much for letting me choose my thesis topic and decide how to manage the progress of the thesis. It was the most meaningful two years in my life. Also, I would like to thank my colleague and more than that, my friend, Ph.D. Hristo Valtchanov. In some way you are like another mentor to me that gives me advice and sets up the plans. I really admire your erudition and appreciate your patience. Thank you so much and like you said, I would pass on this mentorship and enthusiasm to my friends and if possible, my colleagues and students in the future.

In addition, I would also like to thank my parents and my girlfriend, Xiaofan Wang, and all my families and friends. It has been a hard time for all of us because of the COVID-19. Thank you so much for your accompany and support that I could possibly get through this special situation.

Table of Contents

LIST OF ABBREVIATIONS

Abbreviation	**Meaning**
CFD	Computational Fluid Dynamics
LVAD	Left Ventricular Assist Device
CVD	Cardiovascular Disease
CO	Cardiac Output
HR	Heart Rate
SV	Stroke Volume
HF	Heart Failure
CHF	Congestive Heart Failure
NHANES	National Health and Nutrition Examination Survey
AHA	American Heart Association
NYHA	New York Heart Association
ACC	American College of Cardiology
MCS	Mechanical Circulatory Support
BTT	Bridge to Heart Transplantation
BTR	Bridge to Myocardial Recovery
DT	Destination Therapy
IP	Implanted Pneumatic
VE	Vented Electric
INR	International Normalized Ratio
DOP	Design Operating Point

TORVAD	Toroidal Ventricular Assist Device
MPC	Methacryloyloxyethyl Phosphorylcholine
FREE-D	Free-range Resonant Electrical Energy Delivery
RBC	Red Blood Cell
HI	Hemolysis Index
RSM	Reynolds Stress Model
LES	Large Eddy Simulation
DES	Detached Eddy Simulation
NSGA	Non-dominated Sorting Genetic Algorithm
MOSA	Multi-Objective Simulated-annealing Algorithm

LIST OF FIGURES

LIST OF TABLES

LIST OF SYMBOLS

Symbol	Meaning	Unit
Q	Flow rate	[m^3 s^{-1}, L min^{-1}]
ΔP	Pressure rises	[Pa, mmHg]
η	Hydraulic efficiency	[-]
t	Exposure time	[t]
μ	Dynamic viscosity	[Pa s, cP]
τ	Shear stress	[Pa]
$\dot{\gamma}$	Shear rate	[s^{-1}]
σ	Normal stress	[Pa]
N	Rotational speed	[RPM]

Chapter 1: Introduction

1.1 Motivation

Cardiovascular diseases (CVD) are one of the top ten leading death causes in United States and approximately 17.8 million deaths were related to CVD worldwide in 2017 [1]. In the past few decades, the number of patients suffering from cardiovascular diseases, especially heart failure (HF), has been growing rapidly. Over three million patients had congestive heart failure and the number of new cases is increasing over 400,000 per year [2]. Therefore, many mechanical circulatory supports (MCSs) have been developed including stents and left ventricular assist devices (LVADs). These devices can be implemented as bridge to myocardial recovery (BTR), bridge to heart transplantation (BTT) and destination therapy (DT) for patients with Class III and Class IV HF whose life expectancy and quality has been significantly improved. However, there are multiple adverse events such as infections, thrombosis, and hemolysis. It has been shown that these postoperative complications are related to the implementation of LVAD since long time continuous exposure of blood to the rotor would cause accumulated damage to blood cells [1, 2].

1.2 Project Background, Research Objectives, and Thesis Overview

The starting point of this thesis is based on the novel configuration of LVAD as shown in Figure 1.1, a hubless axial flow blood pump [4].

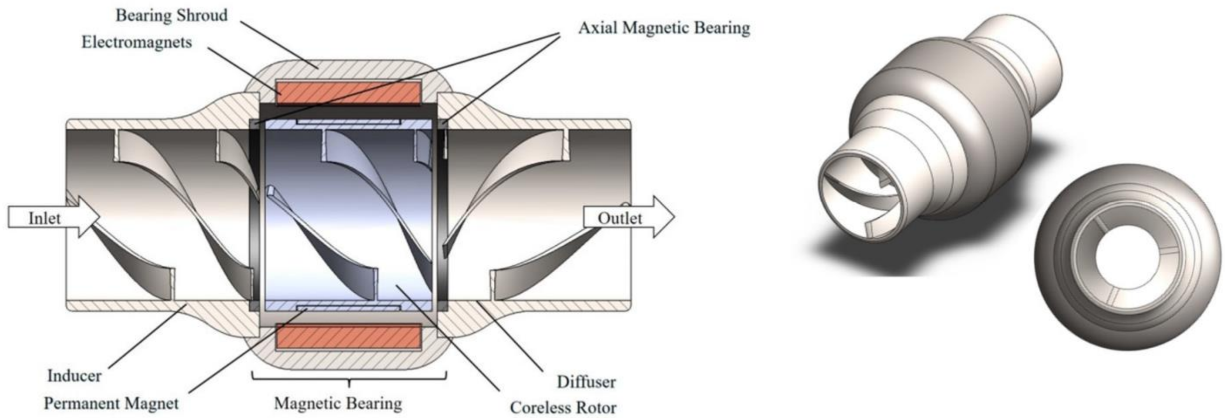

Figure 1.1: Hubless LVAD configuration (left) and isometric and front view (right). Reprinted with permission from [5]

The feature of this novel design is that the blades are mounted on the inner shell of the pump instead of on the hub like conventional axial flow pump. Previous work had found that it could be operated at a much lower rotational speed while maintaining high flow rate due to the higher pumping volume per unit time [3-5]. Conventional axial flow and centrifugal flow pump are shown in Figure 1.2 below.

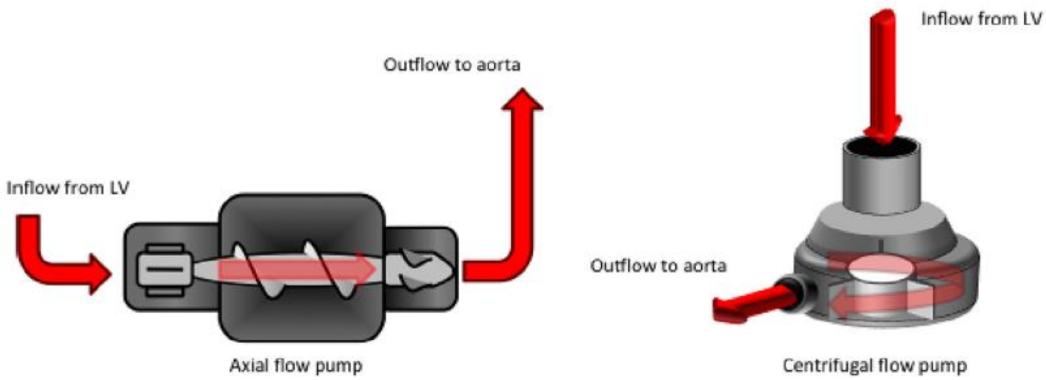

Figure 1.2: Schematics of conventional axial flow pump (left) and centrifugal flow pump (right). Adapted from [6]

As a result, postoperative complications including thrombosis and hemolysis caused by high operating rotational speed could be possibly mitigated. Therefore, the novel design opens the possibility to reduce the blood damage caused by the implementation of LVADs and improve patients' life expectancy and quality. Moving on, Prof. Rosaire Mongrain and his team came out the idea of implementing a secondary diffuser, or the internal volute, to guide the blood flow, as shown in Figure 1.3, to recover the pressure and increase its hydraulic efficiency [5].

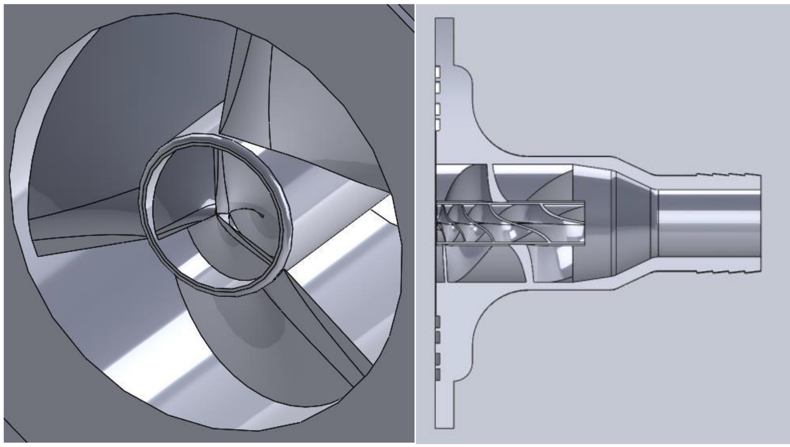

Figure 1.3: Inlet of diffuser (left) and side view of diffuser part (right). Reprinted with permission from [5]

The objective for the thesis is to provide numerical verification and optimization for current LVAD design with implementation of the secondary diffuser. The evaluation goals have been set to maximize the pressure rise and hydraulic efficiency as well as minimize the shear stress and hemolysis index. In this project, CAESES (Friendship System, Potsdam, Germany) is used as a parametrization and optimization tool and ANSYS CFX (ANSYS Inc., Pennsylvania, USA) is selected for Computational Fluid Dynamics (CFD) analysis.

The first chapter of the thesis introduces the motivation and background of the project. The secondary chapter provides literature review for the project including blood properties and modelling, hemolysis indices evaluation methods, CFD basics and optimization methods. Chapter three elaborates the automation setup in ANSYS CFX and CAESES as well as the boundary conditions used for CFD analysis. In addition, the independent parameter groups are also discussed in methodology section. Chapter four summarizes and discusses the results from the optimization and CFD analysis including how design parameters possibly affect the evaluation goals. Chapter five demonstrates the limitations of the optimization methods and results and future work to further verify the LVAD configuration.

Chapter 2: Literature Review

2.1 Cardiovascular Basics

This section provides the fundamental knowledge of the heart, blood properties and hemolysis index evaluation methods. Based on the information from this section, the initial design operating point (DOP) of LVAD was defined, including the geometry dimensions, operating flow rate and blood modeling in CFD analysis.

2.1.1 Physiology of the Heart

The heart is one of the most important organs in human's body and it is located in the middle compartment of the chest. The heart pumps blood through blood vessels to the rest of body carrying oxygen and nutrients. There are four chambers in a human heart: upper left and right atria, and lower left and right ventricles. The left atrium receives the oxygen-rich blood from upper body and sends it to the left ventricle. Then the oxygenated blood is pumped by the left ventricle through aorta to the systemic circulation. In the meantime, the right atrium receives the oxygen-free blood and sends it to right ventricle in order to pump it into pulmonary circulation through lungs (Figure 2.1). The carbon dioxide will be released while oxygen is received into the blood. Therefore, pulmonary circulation and systemic circulation makes up of the circulatory system in human body [7].

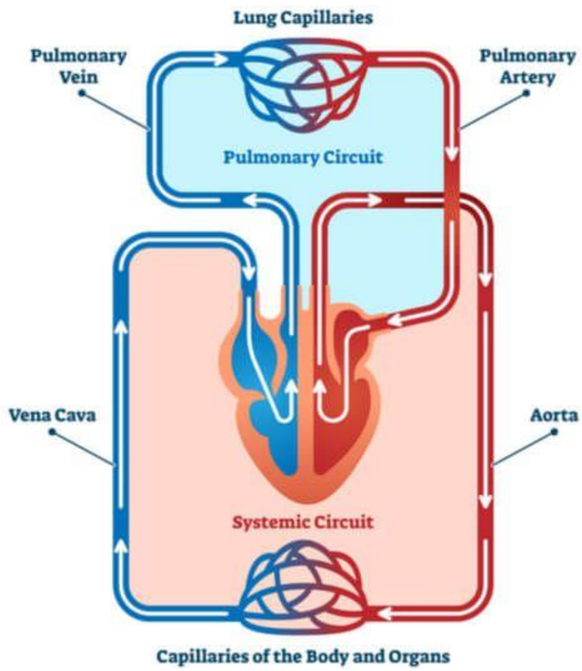

Figure 2.1: Pulmonary circulation. Adapted from [7]

The left heart consists of left atria and ventricle as well as the tricuspid valve to prevent the blood backflow into other cavities. Similarly, right atria and ventricle and mitral valve comprised right heart [8]. There are two periods in a complete cardiac cycle, diastole and systole, corresponding to relaxation period and contraction period, respectively. Systole is defined as the period that the blood is ejected into the rest of the body, while during diastole, the ventricle receives blood from the body and is filled with blood. While during systole, the tricuspid and mitral valve prevent backflow of blood from the ventricles to the atria, the semilunar valves, including aortic and pulmonary artery valves, prevent the backflow from pulmonary and aorta into the ventricles during diastole [9]. The anatomy of the human heart is shown in Figure 2.2.

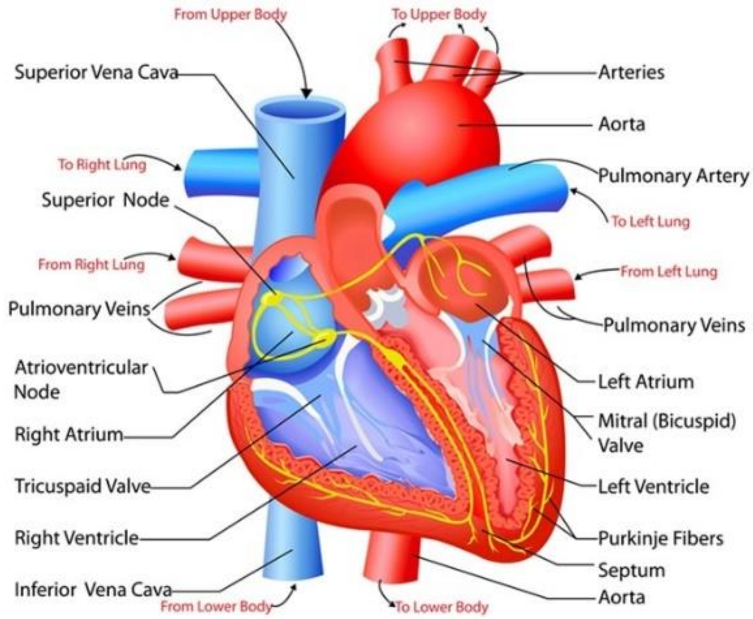

Figure 2.2: Anatomy of the heart with illustrations. Adapted from [8]

The Wiggers diagram is a one of the fundamental tools in cardiovascular physiology, first introduced by Dr. Carl Wiggers [10]. In the Wiggers diagram, as shown in Figure 2.3, the x-axis is time, while the y-axis contains several elements including aortic pressure, ventricular pressure, atrial pressure, ventricular volume and electrocardiogram. Aortic pressure is one of the key elements for designing the LVAD, with the mean diastolic and systolic pressure at rest condition being 80 mmHg and 120 mmHg, respectively.

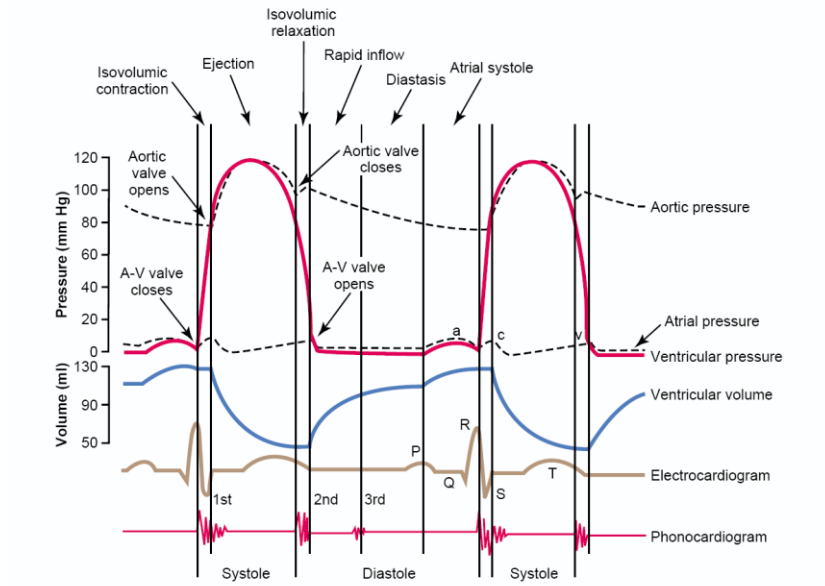

Figure 2.3: Wiggers diagram showing cardiac cycle for left ventricle function. Reprinted with permission from [9]

Cardiac output (CO) describes the volume of the blood pumped by heart per unit time. It is calculated by the product of heart rate (HR) and stroke volume (SV), denoted as CO = HR x SV. Therefore, CO depends on a person's physical characteristics including size of heart, age, possible cardiovascular diseases, and metabolism. The average CO of an adult at rest is 5 L min^{-1}, while it can be increased up to 20 L min^{-1} during exercise [9].

2.1.2 Heart Failure

Congestive heart failure (CHF) is one of the common forms of cardiovascular disease. It occurs when the heart muscle is unable to pump enough blood to the rest of body and potentially cause severe consequences [11]. In the U.S., 6.2 million adults over age of 20 had HF based on the data from National Health and Nutrition Examination Survey (NHANES) 2013 to 2016. Comparing to the data of 5.7 million from 2009 to 2012, the number of patients increases by approximately 10% [1, 12].

Generally, HF can be categorized into two ways: by New York Heart Association (NYHA) from Class one to Class four and by American Heart Association (AHA)/American College of Cardiology (ACC) from Stage A to Stage D. The NYHA classification is based on typical symptoms of HF, from no restriction of exercise at Class one to fatigue and shortness of breath at rest at Class four. On the contrary, AHA/ACC classification is based on possible risks or existing evidence of heart from high risk of developing HF without evidence of cardiac structural changes at Stage A to advanced structural disease in heart at Stage D [11-14]. The treatment options depend on the stage from changing lifestyle in early stages to heart transplant in later stages. For patients with end-stage heart failure, however, the number of donor heart is limited. For example, the median waiting time for a heart transplant during 2011 to 2014 ranged from 72 days to 349 days based on different age group [15]. As the wait time increase, the survival rates for patients could reduce significantly [14, 15]. Therefore, there is an urgent need to develop safe and effective mechanical circulatory support to improve survival while waiting for a heart transplant.

2.2 Left Ventricular Assist Devices (LVADs)

This section provides the historical review for development of LVAD since 1980s, including the techniques each generation of LVAD used as well as the comparison among LVAD from different manufacturers.

2.2.1 Historical Review

First Generation

The first generation of LVADs is characterized by using a pulsatile volume displacement mechanism. It applies pneumatical or electrical forces on pusher plates or actuated sacs to induce pulsatile flow; this generation of LVADs can be implanted intracorporeally or extracorporeally. There were some limitations including infections, thrombosis, and blood trauma. One of the main reasons to cause infections is the large contacting surface between mechanical parts and blood and tissue. This limitation made the device difficult to fit in the hearts of many patients and accelerated the mechanical failure of the parts within two to three years.

One of the typical products of this generation is HeartMate I, which later evolved into HeartMate XVE. It was first developed by Thermo Cardiosystems Inc. (TCI) and put into clinical use in 1986 [16, 17]. HeartMate I was available in both implanted pneumatic (IP) and vented electric (VE) types of devices. There was an external control system inducing the pumping while the blood was channelled into the device through inflow conduit attached to left ventricle and blood was propelled out through an outflow conduit attached to the aorta by pressurizing the blood with a pusher plate. HeartMate XVE was involved in a Randomized Evaluation of Mechanical Assistance for the Treatment of Congestive Heart Failure (REMATCH) study and the result shown that comparing to optimal therapy, HeartMate XVE improved patients' survival rate by 48% [18]. Since received approval from US Food and Drug Administration (FDA) in 2003, HeartMate I (including HeartMate XVE, shown in Figure 2.4) has been applied on over 4500 patients worldwide [16].

Figure 2.4: Picture of HeartMate XVE. Adapted from [17]

Another first-generation device is EXCOR by Berlin Heart. EXCOR is pneumatically actuated, paracorporeal LVAD capable of both left and right ventricular support for adults and children. It has a wide range of ejection volume including 10, 20 and 35 ml for children and 50, 60 and 80 ml for adults, reaching a maximum flow rate of 10 L/min at beat rate of 150. Although all of the blood contact surfaces have been coated with heparin, anticoagulation medicine is recommended to maintain a relatively high international normalized ratio (INR) of 3 to 3.5 [19]. Berlin Heart has obtained the CE mark in 2000 and approval from FDA for paediatric use in 2008. There are over 2000 patients who have been implanted with EXCOR since the approvals [16].

Second Generation

Different from the first generations of LVADs, the second generation used continuous rotary pump instead of a pulsatile volume displacement mechanism. The advantages of non-pulsatile devices included mechanical durability and small size making it possible to be fully implanted. In addition, the electrical power needed for the device was reduced compared to the previous generation, which also reduced the possibility of device-induced infections. There are three categories of continuous flow devices depending on the directions of inlet and outlet: axial flow, radial flow, and mixed flow. Although continuous flow mechanism has solved some of the issues occurs in the first-generation LVADs and infection rate has been reduced, however, due to blood immersed bearing impeller support, the parts still tended to wear out in five years [16].

For axial flow pump, there is an impeller rotating generally at speed between 6000 to 15000 rpm to provide blood to the patient's body. One of the most successful products is HeartMate II, which was first developed by Nimbus Corporation with the University of Pittsburgh. It consists of the pump, controller module, and power base with portable battery [20]. Comparing to HeartMate XVE with a size of 40 mm x110 mm in diameter and a weight of 1190 g, HeartMate II only has a size of 40 mm x 60 mm in diameter and weight of 375 g. With one eighth size of previous generation, it still has the same output capacity [21]. It was reported by several single-center and multicenter studies that the one-year survival rate for 43 patients was 80% as both BTT and DT. Based on different individual managements in different centers, the one-month, six-month survival rates and possibility of adverse events varied. According to the research for 32 BTT patients, one-month and six-month survival rate were 96.9% and 86.9%. Major adverse events including bleeding requiring re-exploration (15.6%), right ventricular failure (6.3%), infection (12.5%) and gastrointestinal bleeding (15.6%) were found [20]. According to another research conducted in an observational multicenter clinical trial, 100 patients out of 133 survived in 180 days after implanting HeartMate II and adverse events including bleed, stroke and right ventricle failure were significantly lower than reported in HeartMate XVE [22]. The schematic of HeartMate II is shown in Figure 2.5.

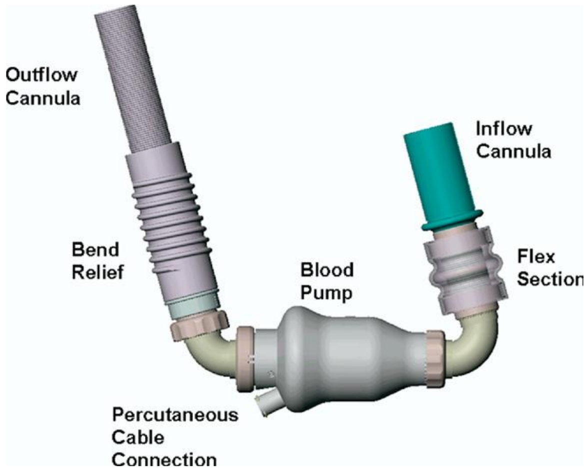

Figure 2.5: Schematic of HeartMate II. Adapted from [20]

Another typical second-generation LVAD is Jarvik 2000 FlowMaker first developed by Dr. Robert Jarvik. It consists of an axial flow pump, a 16-mm outflow graft, a pump-speed adjusting controller and a power supply. It has lighter weight and smaller size than HeartMate II with a weight of 90 g and a diameter of 25 mm. The rotor speed can be adjusted from 8000 to 12000 rpm with an average flow rate of 3 to 7 L min^{-1}. Several single center and multicenter has reported that Jarvik 2000 is safe and durable [20]. Over 257 patients were implanted since April 2000 and no failure implantable parts were reported. In addition, there was a patient supported by Jarvik 2000, shown in Figure 2.6, for over seven years. Due to smaller contact between the device and tissue, the risk of infection was also lower for DT patients [16].

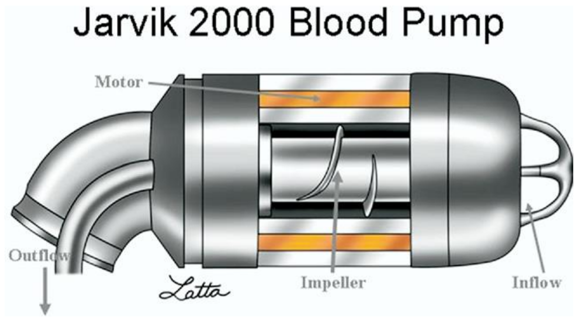

Figure 2.6: Schematic of Jarvik 2000. Adapted from [19]

Third Generation

Based on the second-generation LVADs' limitations, the third generation further reduced the contact between mechanical parts by using magnetic levitation mechanism. Permanent magnets are used to levitate the rotor, replacing standard roller bearings. In addition, the third generation LVAD can also be categorized by the design of motor system including external motor-drive system, direct-drive system and self-bearing or bearingless system [23]. For example, HeartMate III designed by Abbott Laboratories utilized magnetically levitated rotor and the bearingless system to eliminate all friction wear in the parts. There were two versions of HeartMate III, axial flow pump and centrifugal flow pump. The dimensions for centrifugal HeartMate III are 69 mm diameter times 30 mm with a weight of 500 g. Similar to HeartMate II, inflow cannula of HeartMate III is inserted into left ventricular apex and outflow into ascending aorta. Magnetic levitation and motor function are integrated with all control units in the pump's lower housing. In addition, relatively large gaps are used around rotor to keep the surfaces out of the main flow path in order to reduce the risk of thrombosis and hemolysis [24, 25]. Further clinical trials were conducted to compared difference between axial version and centrifugal version of HeartMate III. 1028 patients were involved in which 516 was in the centrifugal pump group and 512 was in the axial pump group. Result shown that 76.9% of patients from centrifugal group and 64.8% from axial group survived and were free of disabling stroke or malfunction of devices at two-year mark. In addition, the number of patients in centrifugal group experiencing pump replacement and major adverse events including bleeding and gastrointestinal hemorrhage was less than the other group [24]. Therefore, HeartMate III with the centrifugal configuration had a better overall performance. The section view of HeartMate III representing its magnetic levitation technology is shown in Figure 2.7.

Figure 2.7: Magnetic levitation technology in HeartMate III. Adapted from [26]

Another third-generation product is InCOR by Berlin Heart. It used direct-drive system and active electromagnetic bearing at the end of rotor to achieve complete rotor suspension. The dimension for InCOR is 120 mm times 30 mm for diameter with the weight of 200 g which makes it the largest axial flow devices. It can support the range of flow rate from 5 to 7 L min^{-1} at the rotor speed of 8000 rpm to 10000 rpm [27]. InCOR also utilized heparin coated with Carmeda on all blood-contacting surfaces to improve its biocompatibility. Also, clopidogrel and dipyridamole as anticoagulation technologies were used to maintain INR range of 2.5 to 3.0, which was similar to the range of other axial flow LVADs. Moreover, based on the clinical data from a multicenter, a modified cannula with extra 10 mm into left ventricular cavity has been used to reduce major adverse events [28]. Since the first clinical trial on human occurred in June 2002, over 500 patients have been implanted with InCOR, as shown in Figure 2.8 [16].

Figure 2.8: Picture of InCOR by Berlin Heart. Adapted from [16]

2.2.2 Current Trend and Development of LVAD

The global LVAD market was estimated to be US $1.2 billion worldwide in 2020. Even within the crisis of COVID-19, the global market was predicted to reach the size of US $2.2 billion by the end of 2027, with the compound annual growth rate of 9.1% during the period of 2020 to 2027. Within the $1.2 billion worldwide market, the U.S. market was estimated at $367.5 million while China, the second largest economy, had the market of 217.8 million with a compound annual growth rate of 8.5% [29-31]. Therefore, great potential growth for LVAD market could be foreseen based on marketing prediction.

There are still several existing challenges for current generation of LVAD including persistent risk of stroke, low lethal hemolysis yet unquantified sublethal hemolysis and right heart failure. A great number of research involving novel improvements are currently undergoing to improve the performance of LVAD as well as minimize the blood damage caused to the patients. For example, the toroidal ventricular assist device (TORVAD) designed by Windmill, shown in Figure 2.9, used synchronous pulsatility and adaptive pumping by sensing cardiac rhythm in order to automatically adjust pump flow rate [32]. In Figure 2.10, LVAD with wave membrane technology designed by CorWave allows for blood flow restoration. Similar to a human heart, it can pump blood without exposing it to the same damage caused by conventional rotary heart pumps [33]. Another example is EVAHEART 2 designed by EVAHEART shown in Figure 2.11. To reduce the possibility of thrombosis and bleeding, both the inner and the outer surface of the impeller are coated with 2-methacryloyloxyethyl phosphorylcholine (MPC) [34].

Figure 2.9: TORVAD designed by Windmill. Adapted from [32]

Figure 2.10: Schematics for CorWave LVAD. Adapted from [33]

Figure 2.11: EVAHEART coating on the impeller surfaces. Adapted from [34]

On the other hand, percutaneous drivelines of LVAD could cause infections and bleeding and limit patients' mobility and life quality [35, 36]. Therefore, research focusing on improving the power transmission system as well as eliminating the drivelines to reduce the infections is being investigated. For example, the Free-range Resonant Electrical Energy Delivery (FREE-D) wireless power system has been testing and under development. Similarly, the new wireless power transfer technology designed by LeviticusCardio Ltd. was tested and integrated with Jarvik 2000, designed by Jarvik Heart Inc., to obtain clinical statistics [37].

In conclusion, depending on diverse aspects focused by various companies, the improvement of the current LVAD technology can be categorized as reduction in blood damage (hemolysis, thrombosis, etc.), limitation of its size, and elimination of percutaneous drivelines (infections).

2.3 Blood Physiology and Prediction of Blood Damage

This section introduces the basic properties of blood and red blood cell. In addition, it also provides the methods for estimation of hemolysis indices that will be used for calculation in the later chapters.

2.3.1 Mechanical Properties of Blood and Red Blood Cells

Blood is a fluid connective tissue made up of cellular components and extracellular elements. Cellular components are comprised of red blood cells (RBCs), white blood cells (WBCs) and platelets while extracellular element is plasma, which is a water solution of proteins and nutrients with myriad important physiological roles [9]. On average, the density of human whole blood is 1056 kg m^{-3} [38]. Dynamic viscosity of blood, normally represented by μ, varies based on the level of hematocrit with a range between 3.23 x 10^{-3} Pa s to 4.20 x 10^{-3} Pa s [9, 39]. Under natural conditions, it is a non-Newtonian fluid with shear thinning properties. To be specific, its dynamic viscosity decreases with increasing shear rates as shown in Figure 2.12.

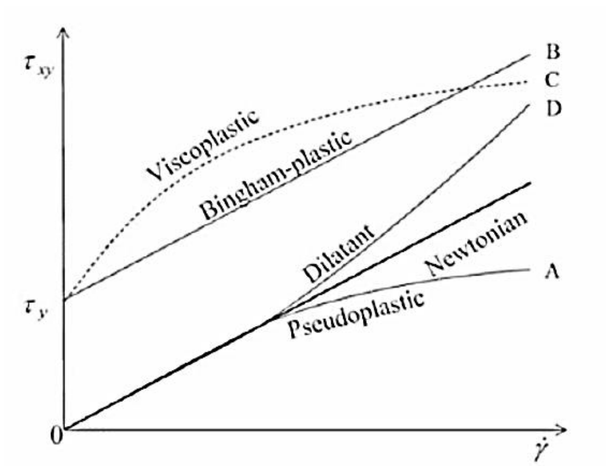

Figure 2.12: Shear stress versus shear rate for different fluids. Adapted from [40]

However, when the blood is exposed to high shear rates above 100 s^{-1}, the dynamic viscosity can be considered as Newtonian. For this reason, as the near-wall shear rates in LVADs generally range from 10^2 to 10^5 s^{-1}, whole blood can be modeled as a Newtonian fluid with minimal impact on the magnitude and distribution of predicted shear stresses at the wall [41-43]. While performing CFD analysis, blood is generally modeled as an incompressible fluid with constant dynamic viscosity of 3.5 x 10^{-3} Pa s under body temperature of 37 Celsius [44, 45]. Therefore, the shear stress can be calculated by Equation 2.1:

$$\tau = \mu \dot{\gamma} \tag{2.1}$$

where τ is the shear stress [Pa], τ is the dynamic viscosity of blood [Pa s] and $\dot{\gamma}$ is the shear rate [s^{-1}]. The viscosity measurement of human blood versus different shear rate under room temperature is shown in Figure 2.13.

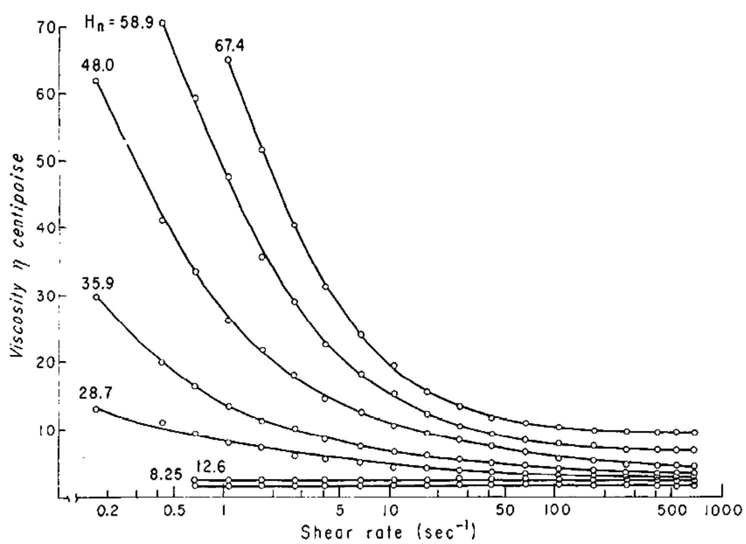

Figure 2.13: Relationship between viscosity and shear rate under room temperature with varying volume concentration of the erythrocytes. Reprinted with permission from [43]

Red blood cells (RBC), or erythrocytes, are membranous sacks filled with concentrated hemoglobin solution. The main function of RBC is to bind the oxygen in the lung and transport it to the rest of body, and then carry carbon dioxide back to lung for the circulation [46]. In natural condition, RBC has a biconcave disk shape with no nuclei inside the cell. The average size for RBC is 7.5 μm in diameter with the normal range of 6.2 μm to 8.2 μm and 2.0 μm for thickness with the normal range of 2.0 μm to 2.5 μm as shown in Figure 2.14 [47].

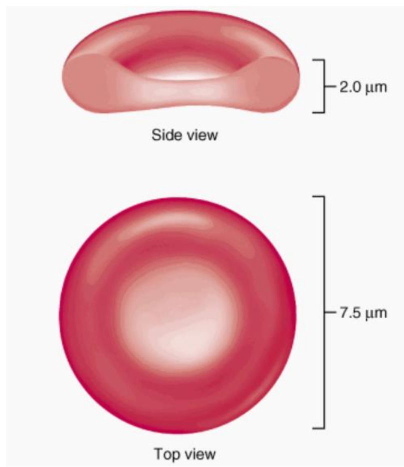

Figure 2.14: Schematic and dimensions for a typical RBC. Reprinted with permission from [46]

Under different shear rate environment or passing through capillaries, since the capillaries normally have smaller diameter than RBCs, the RBCs could deform and show various characteristics. For example, when the RBC is unstressed, rouleaux formation emerges due to stacking RBCs. Under small shear rates, normally less than 1 s^{-1}, the cell will tumble [48, 49]. Next, when shear rate is over 1.5 Pa s, RBCs will deform into ellipsoidal shape with oriented arrangement. When shear rates keep increasing, the ellipsoidal shape will be elongated, and RBCs will be hemolyzing. There would be pores formed on the membrane of RBC and cause sublytic hemoglobin release. Different from hemolysis that causes fully rupture of RBC membrane, sublytic or hemolyzing state refers to the partial hemoglobin releasing from the pores [49]. The complete process of increasing shear rate environment is shown in Figure 2.15.

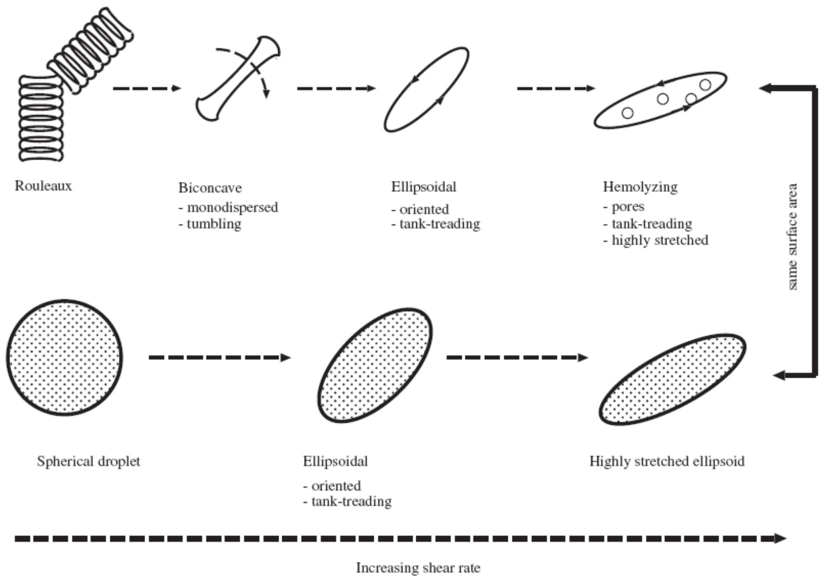

Figure 2.15: RBC and droplet deformation with increasing shear rate environment. Adapted from [48]

Healthy RBCs usually have a lifespan of 100 to 120 days [50, 51]. As the cells age, their properties such as volume, surface area, and relaxation time also change [52, 53]. In addition, it is believed that the contact with mechanical circulatory devices such as LVAD could cause sublethal trauma and speed up the aging effect [54].

2.3.2 Hemolysis Indices (HI)

Hemolysis index (HI) is an indicator to evaluate ratio of extracellular hemoglobin to intracellular hemoglobin coming from ruptured or damaged red blood cell membranes (lethal or sublethal). It is defined by Equation 2.2:

$$HI\ [\%] = \frac{\Delta Hb}{Hb} \times 100 \tag{2.2}$$

where ΔHb is the change of extracellular hemoglobin and Hb is the total hemoglobin concentration, both with the unit of [g/L] [55].

The experimental data was conducted by Giersiepen M. and Wurzinger, L. J. in 1990 under shear stress variation up to 255 Pa and exposure time up to 0.7 s with Couette-viscosimeter. It has been proved to be the gold standard for hemolysis evaluation. By fitting the experimental data, the Giersiepen-Wurzinger equation has been defined as Equation 2.3:

$$HI = 3.62 \times 10^{-5} \times \tau^{2.416} \times t^{0.785} \tag{2.3}$$

where τ is shear stress scalar [Pa] and t is exposure time [s] [56]. The general equation of HI is shown in Equation 2.4:

$$HI = C\ \tau^{b} \times t^{a} \tag{2.4}$$

where constants are replaced by C, a, and b for repeated experiments with blood of other species. For porcine, the experiments had a shear stress range of 30 Pa to 600 Pa and exposure time of 0.0034 s to 0.69 s. For ovine experiment, range for shear stress was 30 Pa to 320 Pa and exposure time was 0.03 s to 1.5 s [45]. The constants fitting by experimental data for human blood and animal blood are listed in Table 2.1.

Table 2.1: Constants for human blood, porcine and ovine [45]

	C [Pa^{-b} s^{-a}]	a [-]	b [-]
Human [45]	3.63×10^{-5}	2.416	0.785
Porcine [57]	1.8×10^{-6}	1.991	0.765
Ovine [58]	1.288×10^{-5}	1.9918	0.6606

2.4 Computational Fluid Dynamics (CFD) and Optimization Algorithms

This section provides the fundamental knowledge of Computational Fluid Dynamics (CFD) and the optimization algorithms used in later chapters to analyze the simulation results.

2.4.1 Computational Fluid Dynamics (CFD) Basics

Computational Fluid Dynamics (CFD) is a computer-based design and research tool for mathematically modeling and simulating fluid flow systems. It is based on the fundamental governing equations including continuity, momentum, and energy equations. With the specifications of known conditions, or boundary conditions, it can generate a numerical solution and perform further analysis for a given system. The first governing equation in fluid dynamics is the continuity equation. It is shown in Equation 2.5:

$$\frac{\partial \rho}{\partial t} + \nabla \cdot (\rho U) = 0 \tag{2.5}$$

where ρ is density [kg m^{-3}], t is time [s] and U is fluid velocity [m s^{-1}]. For incompressible fluid with constant density everywhere, Equation 2.5 can be simplified to Equation 2.6 as shown below:

$$\nabla \cdot U = 0 \tag{2.6}$$

The next governing equation is the conservation of momentum equation based on Newton's second law shown in Equation 2.7:

$$F = ma \tag{2.7}$$

Then by calculating body forces and surface forces on x, y and z direction, the momentum equation can be summarized with index notation shown in Equation 2.8 [61]:

$$\frac{\partial}{\partial t}(\rho u_i) + \frac{\partial}{\partial t}(\rho u_i u_j + p\delta_{ij} - \tau_{ij}) = 0 \tag{2.8}$$

where i = 1, 2, 3; ρ is the density [kg m^{-3}], P is pressure [Pa] and τ is shear stress [Pa].

In this thesis, ANSYS CFX (ANSYS Inc., Canonsburg, PA) is used as the primary CFD tool. As shown in Figure 2.16, the CFD process starts from geometry and mesh generation. Then in CFX-Pre, the boundary conditions including analysis type, inlet and outlet definition and subdomains can be set up. Lastly, user can generate result reports and perform post processing analysis in CFD-Post.

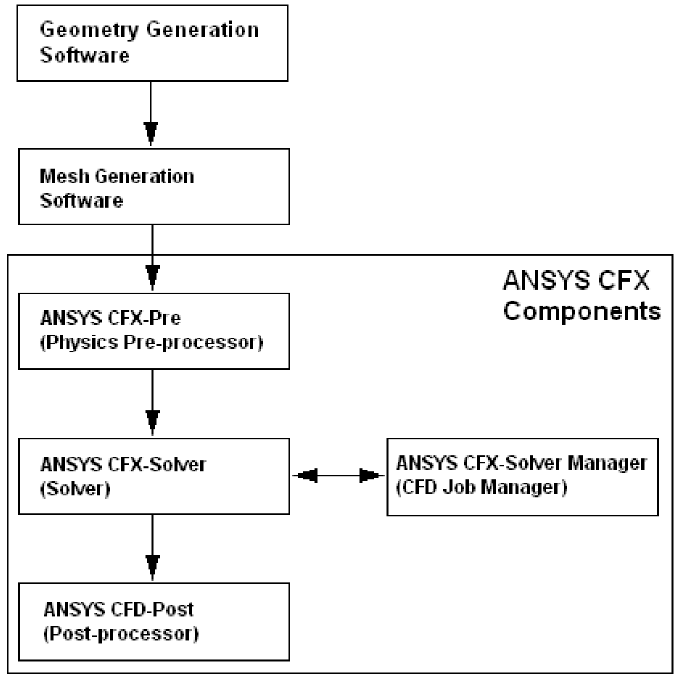

Figure 2.16: CFD analysis process for ANSYS CFX. Adapted from [62]

Besides the governing equation for solving the system, the turbulence models are also provided in ANSYS CFX. In general, for a straight pipe flow, if the Reynolds number is smaller than 2000, the flow can be considered as laminar flow while if Reynolds number is greater than 4000, it is turbulent flow. For the Reynolds number falling between the range of 2000 to 4000, the flow can be considered as transitional flow [63]. In the case of LVADs, it is turbulent flow since Reynolds number is higher than 4000 due to the highly complex geometry. ANSYS CFX provides multiple turbulence models including Eddy-viscosity models, Reynolds stress models (RSM), Large Eddy Simulation (LES) and Detached Eddy Simulation (DES) turbulence models [62]. In hemodynamic studies, k-ω shear stress transport (SST) turbulence model has been found to be able to capture the flow transition from laminar to turbulent. In addition, k-ω SST can predict wall shear stress better than standard Reynolds-averaged Navier-Stokes (RANS) based turbulence model [64].

Moreover, it has been proved that k-ε model is not accurate to handle low turbulent Reynolds number computations. To have a better prediction for wall functions, ANSYS CFX used ω related equations including standard k-ω, Baseline k-ω and ω-Reynolds Stress for near wall boundary conditions as automatic near wall treatment [61]. Therefore, k-ω SST turbulence model was used for further CFD simulations and details will be discussed in future chapters.

2.4.2 Design Exploration Algorithms

One of the most common design exploration algorithms is the random number generators (RNGs). RNG is a process of generating a sequence of numbers that cannot be predicted. There are two types of RNG: hardware random number generator (HRNG) and pseudorandom number generator (PRNG). HRNG generates true random numbers by using unrepeatable and unpredictable physical environment attributes while PRNG generates the random number that can be possibly reproduced if the PRNG states are obtained [65]. PRNG have been used in many applications including computer simulations and crypto systems [66]. Sobol sequence is one of the quasi-random (QR) sequence designed to generate a uniformly distributed number within the given range [67]. The comparison between random sequence and Sobol sequence is shown in Figure 2.17.

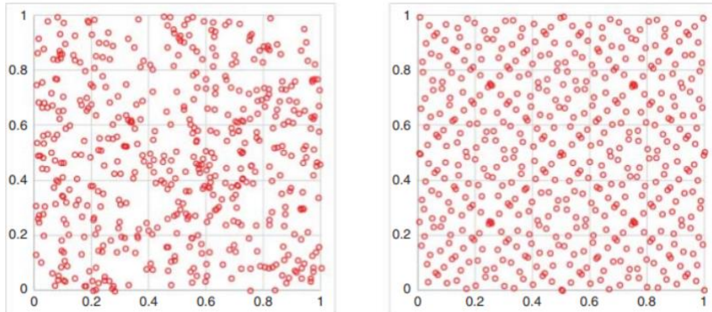

Figure 2.17: Comparison between random sequence (left) and Sobol sequence (right). Reprinted with permission from [68]

In addition, the Sobol sequence is able to reduce clusters and hollow area and has better convergence comparing to random sequences [69]. A multitude of standard optimization tools are readily available in commercial optimization software such as CAESES, which was used in this thesis, including Tangent Search, Brent, Newton-Raphson, and Nelder-Mead Simplex for single objective optimization and Non-dominated Sorting Genetic Algorithm (NSGA II), dominance-based multi-objective simulated-annealing algorithm (MOSA) and Response Surface Optimization for multi-objective optimization. Sobol sequence is usually selected as the method for the first stage of an optimization, more specifically, the design exploration study method. Then it can be followed by single or multi-objective methods to further achieve optimal point design evaluation goals. Therefore, in this thesis, Sobol was used as the main optimization algorithm and will be further elaborated in the future chapters.

Chapter 3: Methodology

3.1 Initial Geometry Definition

This section provides the initial definition of the geometry used in optimization, including implementation of secondary diffuser, fluid domain subtraction and rebuilt of fluid domain in CAESES.

An open hub LVAD being developed internally at McGill with secondary diffuser is shown in Figure 3.1.

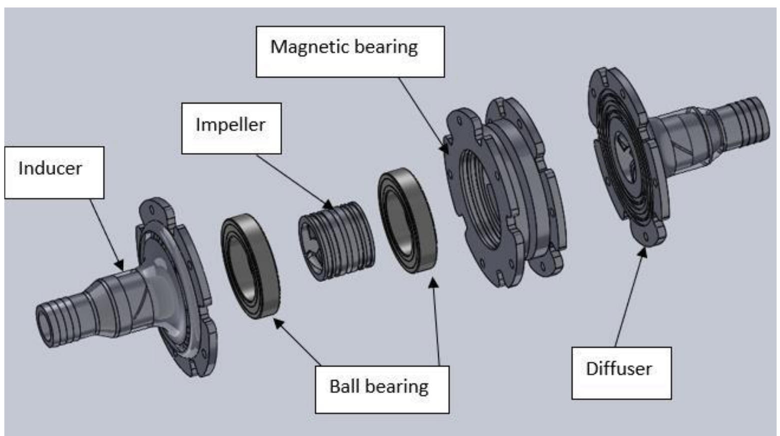

Figure 3.1: Exploded view of LVAD design by Prof. Mongrain's and Dr. Cecere's team. Reprinted with permission from [5]

To perform CFD analysis, fluid domain of the new design of LVAD is required and was built in CAESES with the parameters shown in Table 3.1.

Table 3.1: Baseline design variable values for inducer, impeller, diffuser, and secondary diffuser

Part	Parameters	Value	Units
Inducer	Number of blades	3	-

(Stator)	Number of turns	0.4	-
	Blade width ratio	0.5	-
	B-spline parameter x	0.5	-
	B-spline parameter y	0.5	-
	Start angle	0	degree
	End angle	0	degree
	Blade position offset angle	0	degree
	Connection thickness	1	mm
	Blade length	37	mm
	Blade thickness	1	mm
Impeller (Rotor)	Number of blades	3	-
	Number of turns	0.4	-
	Blade width ratio	0.5	-
	B-spline parameter x	0.5	-
	B-spline parameter y	0.5	-
	Start angle	0	degree
	End angle	0	degree
	Blade position offset angle	0	degree
	Connection thickness-Diffuser	1	mm
	Connection thickness-Inducer	1	mm
	Blade length	30	mm
	Blade thickness	1	mm
Diffuser (Stator)	Number of blades	3	-
	Number of turns	0.4	-
	Blade width ratio	0.5	-
	B-spline parameter x	0.5	-
	B-spline parameter y	0.5	-
	Start angle	0	degree
	End angle	0	degree
	Blade position offset angle	0	degree
	Outlet diameter	14	mm
	Outer diameter	30	mm
	Connection thickness	1	mm
	Blade length	37	mm
	Blade thickness	1	mm
Secondary Diffuser (Stator)	Number of blades	3	-
	Number of turns	1	-
	B-spline parameter x	0.5	-
	B-spline parameter y	0.5	-
	Start angle	0	degree
	End angle	0	degree
	Blade position offset angle	0	degree
	Connection thickness	1	mm
	Blade length	37	mm

	Blade thickness	1	mm
	Shroud thickness	1	mm
	Inner solid diameter	0.8	mm

The value of design variables in baseline model were referenced to the fluid domain of previous existing model built in the SolidWorks. Using CAESES, a total number of 48 independent parameters has been defined in the model. CAESES is an optimization and parametrization software that user can update and output new geometry each time by varying design variables. Unlike other common computer-aided design (CAD) software, CAESES allows user to construct boundary representation (BRep) for complex geometry and reduce the number of parameters that are needed to describe a given geometry. One of the advantages of using BRep is that CAESES can regenerate each geometry model much easier in the situation of large number of regenerations in optimization. In addition, it also provides the function of different splines when building up a curve such as basis spline (B-spline). Specifically in this baseline model, B-spline was used to define the blade shape while start and end point of (0, 0, 0) and (1, 1, 0) were fixed. By adding an extra point within the range (0, 1) and varying the value of parameter x and y of this point, the curvature of the blade was also varied, shown in Figure 3.2 below.

Figure 3.2: Comparison between parameter x at 0.1 (left) and 0.9 (right) for diffuser part

For the baseline model, the number of blades for the inducer, impeller and diffuser were set to three and all blade curvature were set to be at a neutral position (parameter x equals 0.5). The length for each parts and the inlet and outlet flow region were obtained directly from previous CAD file, with the total length of 194 mm. The connection thickness, or gap, at the inducer-impeller interface and impeller-diffuser interface was set to 1 mm, to prevent blades from adjacent parts directly contacting each other. The overview of the complete fluid domain is shown below in Figure 3.3.

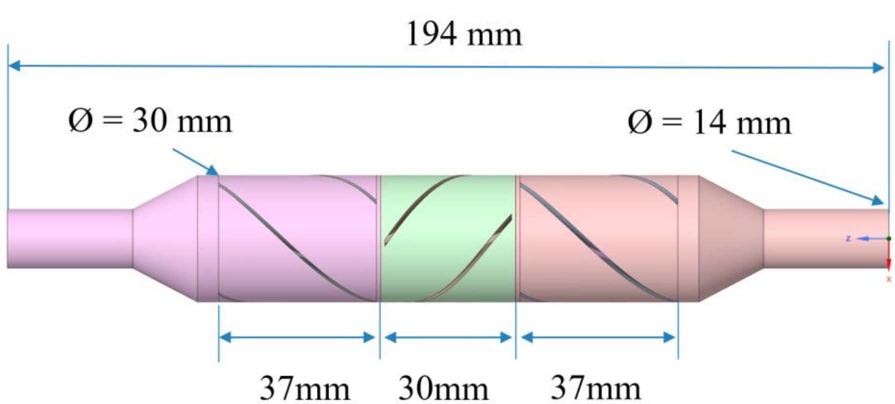

Figure 3.3: The overview of baseline fluid domain built in CAESES

A few assumptions and simplifications were made comparing to the original fluid subtraction from previous CAD model to achieve better mesh and CFD accuracy. First, the inlet diameter was equal to the outlet diameter, so was the length of inlet region before the inducer blade and the length of outlet region after the diffuser blade. Therefore, the inlet and outlet flow regions were relatively symmetric. Also, the secondary blade length was equal to the shroud length since the secondary diffuser blade was mounted on the shroud. Moreover, the inner solid, shown in Figure 3.4, with diameter of 1 mm at the center of secondary diffuser blade was created to avoid potential mesh and CFD calculation errors since the flow in such a narrow tube might trigger mesh generation errors.

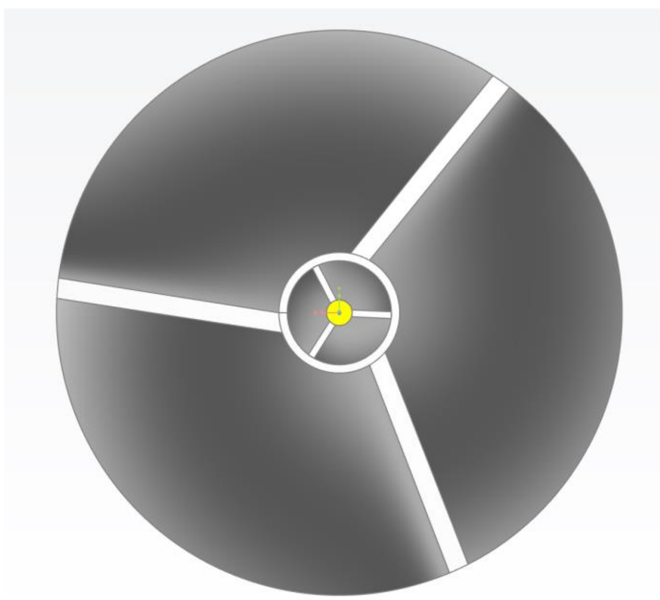

Figure 3.4: Schematic of inner solid generation in the center of diffuser part

3.2 Computational Fluid Dynamics (CFD) Setup

This section provides the details of mesh and computational fluid dynamics setup in ANSYS Mesh and CFX, including mesh sensitivity analysis, boundary conditions and output parameters from Workbench.

3.2.1 Mesh

All of the fluid domains were meshed using mechanical meshing tool with an unstructured advancing front tetrahedral method. Four inflation layers were generated at all blades surfaces with the first aspect ratio set to 15 and a growth rate of 1.2 under smooth settings. There were 2.78 x 10^6 for total number of elements and 6.83 x 10^5 nodes with element size of 0.7 mm. The average element quality was found out to be 0.72 and average skewness was 0.24. The overview and detailed view of mesh are shown in Figure 3.5 and Figure 3.6.

Figure 3.5: Overview of mesh for baseline model

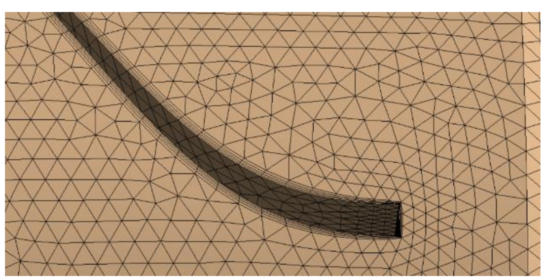

Figure 3.6: Detailed view of mesh at diffuser blade with inflation layers

A mesh sensitivity analysis was performed wherein the range for the number of elements was from ten thousand to nearly ten million when monitoring pressure rise, HI, and average shear stress. The convergence shown in Figure 3.7, Figure 3.8, and Figure 3.9, were monitored.

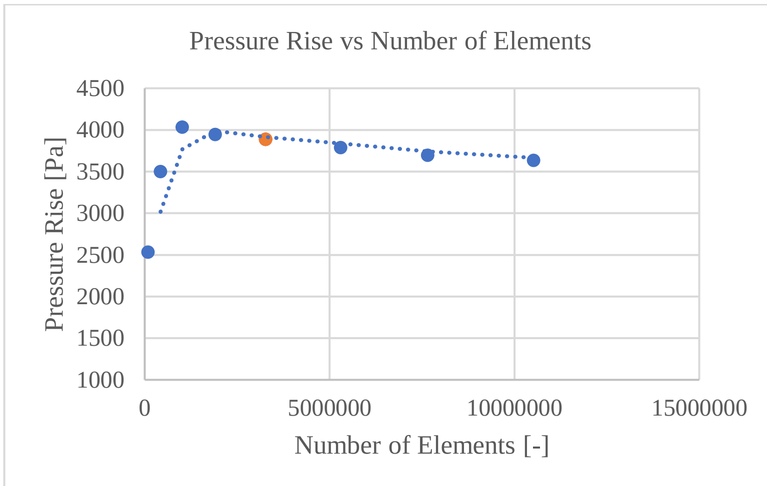

Figure 3.7: Pressure rise versus number of elements

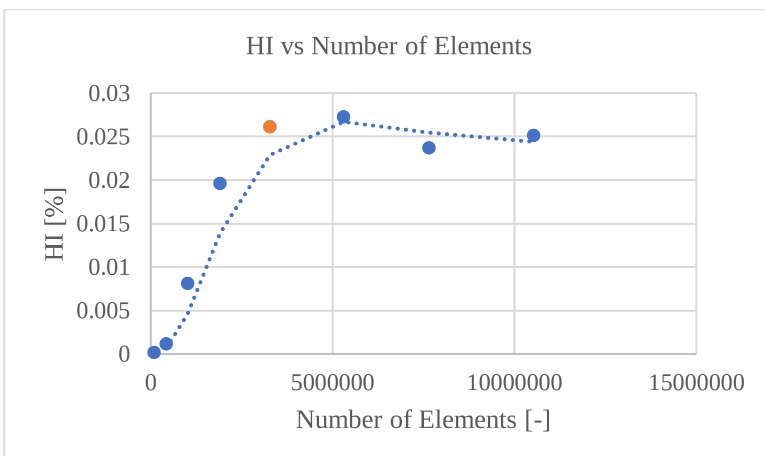

Figure 3.8: HI versus number of elements

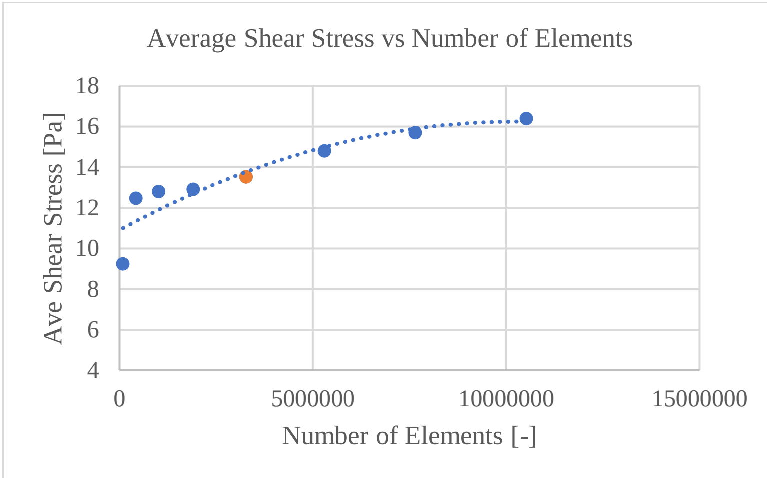

Figure 3.9: Average shear stress versus number of elements

Among three parameters, pressure rise has the best convergence result since it keeps stable after increasing number of elements over around two million. HI also remains stable despite the mild fluctuation at approximately seven million elements with approximately 10% deviation comparing to other data points greater than two million. Average shear stress shows the increasing trend while refining the size of elements. However, it is not the primary objective and the wall function used by ANSYS meshing tool could have a great influence on the accuracy of shear stress evaluation. Therefore, it is reasonable and acceptable to have around 20% deviation. Eventually, the point at three million number of elements showing in the orange dot in the plots was selected considering both result convergence and reasonable simulation computing time.

3.2.2 Boundary Conditions

ANSYS CFX was the software used for performing CFD analysis in during the optimization process. The boundary conditions used in the baseline and all simulations in this work are shown in Table 3.2.

Table 3.2: Summary of boundary conditions in CFX

Solver	CFX	
Analysis Type	Steady State	Transient Total time: 0.3 s Time step: 0.00833 s
Material	Blood (Incompressible liquid) Density 1056 kg/m^3 Viscosity: 3.5 cP Newtonian fluid	
Turbulence Model	Shear Stress Transport (SST)	
Boundary Conditions	Inlet: mass flow rate (flow rate of 5L/min) Outlet: static pressure (0 Pa) Wall: non-slip wall Impeller: rotational speed 2000 rpm Inducer: stationary domain Diffuser: stationary domain	
Interface	Frozen rotor	Transient rotor-stator
Convergence Criteria	RMS < 10^{-4}	
Output Parameters	Pressure rise, hemolysis index, average shear stress, maximum shear stress, and efficiency	

Although the transient setting was set up, most of the optimization simulations used steady state setting mainly because of computational purpose. For transient total time and time step setting, total time was set to 0.3 s. Calculating the time consumed for 10 resolutions under 2000 RPM rotational speed, the individual time step was set to 0.00833 s. The simulation time for one steady state run would take 35 to 40 minutes while the time for transient run was over three and half hours, with the number of elements and all the rest of boundary conditions remaining the same. Therefore, although simulation with transient settings could have a more accurate result and a better convergence with smaller residuals, steady state setting was used for further optimization process due to its acceptable accuracy and significantly shorter computing time.

There were five parameters defined as output evaluation parameters using CFX functions: pressure rise, HI, average shear stress, maximum shear stress and hydraulic efficiency. Inlet-outlet pressure rise was defined by the average pressure difference between outlet surface and inlet surface. HI was calculated by using Giersiepen Wurzinger equation shown in Equation 3.1:

$$\mathrm{HI}\ [\%] = \frac{\Delta \mathrm{Hb}}{\mathrm{Hb}} = 3.62 * 10^{-5} * \tau^{2.416} * t^{0.785} \tag{3.1}$$

where τ is the shear stress scalar [Pa] and t is the exposure time [s].

Since time was a variable in CFD simulations, the integration of $\frac{\mathrm{dHI}}{\mathrm{dt}}$ along the streamlines generated by CFX was used to calculate the final HI value for each geometry variant. In addition, the average and maximum shear stress were calculated by using the function calculator in CFX and averaged over all blood-exposed surfaces in the geometry.

The tensor form of stress can be represented by Equation 3.2:

$$\sigma = \begin{bmatrix} \sigma_{xx} & \tau_{xy} & \tau_{xz} \\ \tau_{yx} & \sigma_{yy} & \tau_{yz} \\ \tau_{zx} & \tau_{zy} & \sigma_{zz} \end{bmatrix} \tag{3.2}$$

In order to obtain a scalar value to plug into Giersiepen Wurzinger Equation and calculate HI, the norm of this stress tensor was taken as shown in Equation 3.3, which is proposed by Bludszuweit et al. [70].

$$\sigma_n = \sqrt{\frac{\sigma_{xx}^2+\sigma_{yy}^2+\sigma_{zz}^2-\sigma_{xx}\sigma_{yy}-\sigma_{zz}\sigma_{yy}-\sigma_{xx}\sigma_{zz}+3(\tau_{xy}^2+\tau_{yz}^2+\tau_{xz}^2)}{3}} \tag{3.3}$$

Lastly, the hydraulic efficiency, η, was defined by the Equation 3.4:

$$\eta = \frac{Output\ Energy}{Input\ Energy} = \frac{\Delta P * Q}{N * \tau} * 100\% \tag{3.4}$$

where ΔP is the pressure rise across the pump [Pa], Q is the volumetric flow rate of the pump [$m^3\ s^{-1}$], N is the rotational speed of the impeller [RPM], and τ is the torque of the impeller [N m].

3.3 Optimization Setup

This section provides the connections between ANSYS Workbench and CAESES and how the parameters are grouped and analyzed during optimization.

3.3.1 Parameter Groups

There were over 50 parameters in total when generating the baseline model. As varying each parameter independently would lead to a prohibitively large parameter space to explore, five independent parameter groups had been created in order to separate parameters into groups that were expected to act together and reduce simulation time. This grouping was intuitively decided based on prior knowledge, a more formal clustering process could be achieved by using a clustering algorithm. 100 simulations were run for each of the parameter group to obtain sufficient data points and create relatively reasonable correlations between each design variable and evaluation parameter. In order to proceed the optimization process, from group one to group five, the individual optima from the previous parameter group was selected and the values were fixed for the running the next group of simulations.

The first group was the blade angle variation including eight parameters of start and end angle for inducer, impeller, diffuser, and secondary diffuser. Running this group could explore the optimal angle combination between the angles for each of the part. The second group was blade geometry variation, including four blade turns and four parameter x, one for each of the part. Blade turn was defined as the angular range between start position and end position of a blade, and one turn was equal to 360 degrees. Parameter x for a blade could define the blade curvature and blade position for a part.

The third group was pump size variation which could control the overall size of the pump. There were nine parameters in total including the outer diameter, outlet diameter, diameter ratio for inducer, impeller, and diffuser, and four connection thickness at two interfaces. The diameter ratio was defined by the shroud diameter over outer diameter. Although there was no shroud for inducer and impeller, the ratio could still vary the blade width in x and y direction.

The last two groups were blade length variation with three parameters for inducer, impeller and diffuser, and number of blade variation with four parameters for inducer, impeller, diffuser, and secondary diffuser. The range for length of each part was based on previous generation of axial-flow LVAD which had a maximum total length of 130 mm. Therefore, the maximum length of each part was controlled to be less than 40 mm. In addition, since increasing the number of blades more than six could significantly increase the shear stress and damage applied on the blood, the maximum number of blades for each part was set to six. The details of independent parameter groups were shown in Table 3.3.

Table 3.3: Details for independent parameter groups

Parameter Groups	**Parameters**
Blade Angle Variation	Inducer Start Angle

	Inducer End Angle
	Impeller Start Angle
	Impeller End Angle
	Diffuser Start Angle
	Diffuser End Angle
	Secondary Start Angle
	Secondary End Angle
Blade Geometry Variation	Inducer Turns
	Inducer Parameter x
	Impeller Turns
	Impeller Parameter x
	Diffuser Turns
	Diffuser Parameter x
	Secondary Turns
	Secondary Parameter x
Pump Size Variation	Outer Diameter
	Inlet/Outlet Diameter
	Inducer Diameter Ratio
	Impeller Diameter Ratio
	Diffuser Diameter Ratio
	Inducer-Impeller Gaps
	Impeller-Diffuser Gaps
Blade Length Variation	Inducer Blade Length
	Impeller Blade Length
	Diffuser Blade Length
Number of Blade Variation	Inducer Number of Blades
	Impeller Number of Blades
	Diffuser Number of Blades
	Secondary Number of Blades

Chapter 4: Results and Discussion

4.1 Parameter Sensitivity Analysis

4.1.1 Pressure Increase

There were seven parameters that have positive effect to pressure rise, as shown in Figure 4.1 to Figure 4.4: pump outer diameter, diffuser number of blades, diffuser blade length, pump inlet/outlet diameter, impeller parameter x, impeller end angle, and impeller blade length. The parameters were ranked by decreasing sensitivity. The target pressure range is to satisfy human's systolic and diastolic pressure 80 mmHg to 120 mmHg, which is equivalent to approximately 10666 Pa to 15999 Pa.

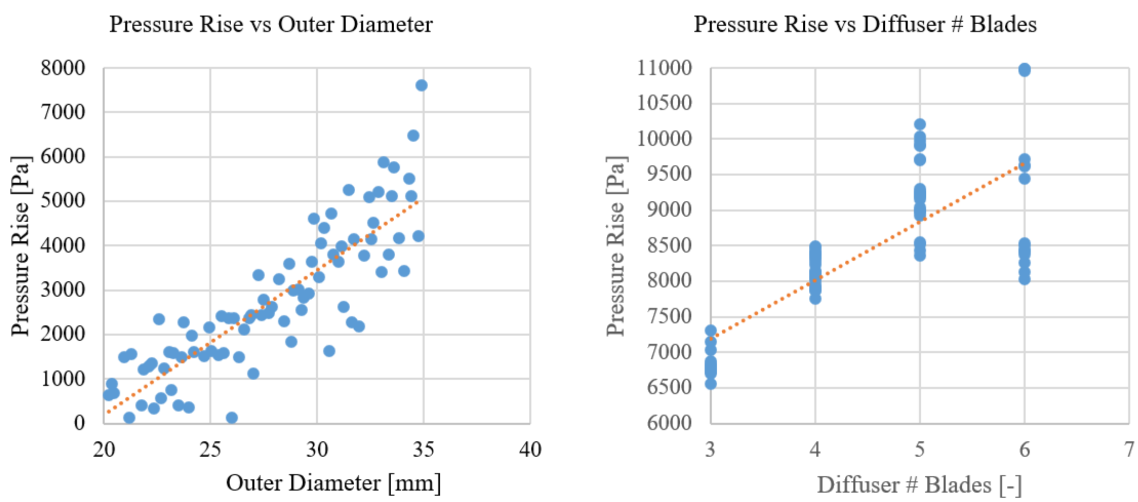

Figure 4.1: Pressure rise versus pump outer diameter (left) and diffuser number of blades (right)

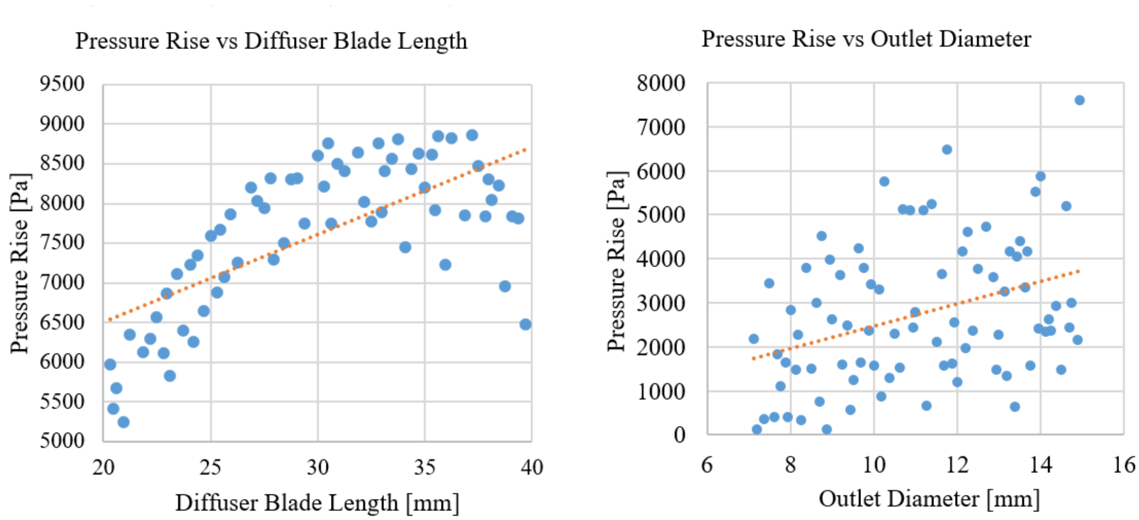

Figure 4.2: Pressure rise versus diffuser blade length (left) and pump outlet diameter (right)

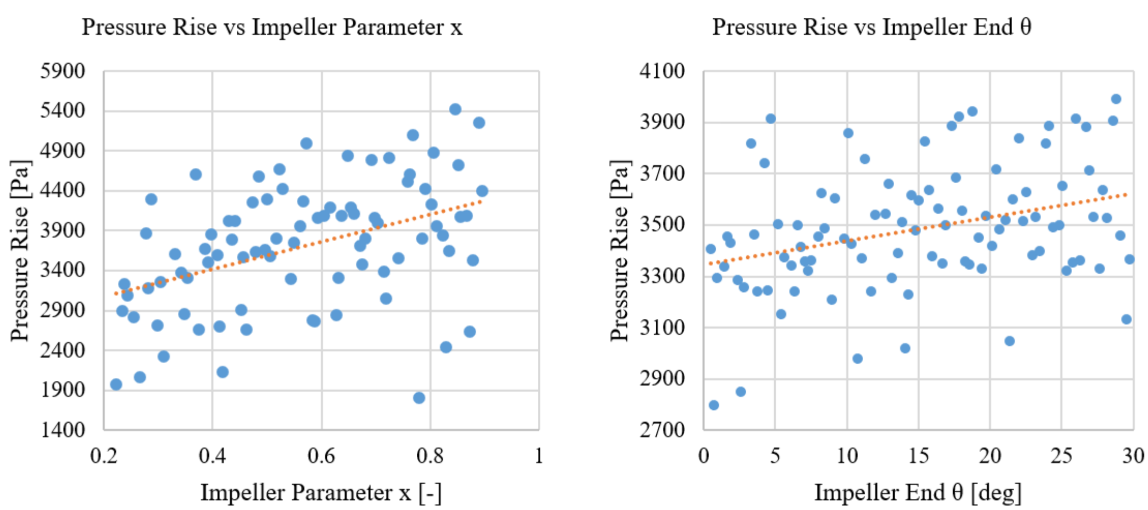

Figure 4.3: Pressure rise versus impeller parameter x (left) and impeller end angle (right)

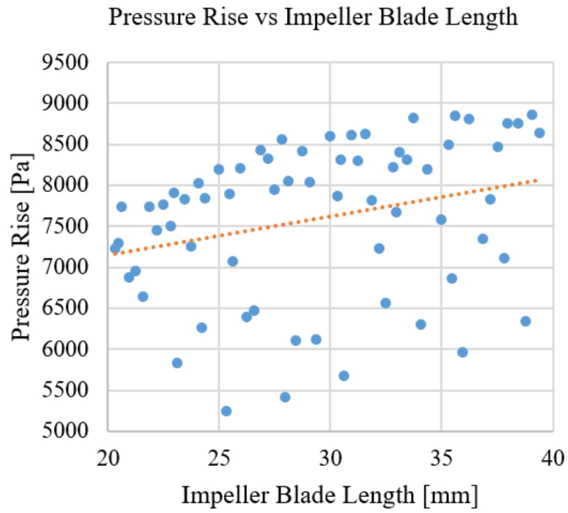

Figure 4.4: Pressure rise versus impeller blade length

The parameters in diffuser and impeller affect the pressure rise the most, including outer and outlet diameter, diffuser number of blades and blade length, impeller parameter x and blade length. Increasing diffuser number of blades and length can better guide the flow and recover the pressure. Changing the blade curvature of impeller parameter x can also help to de-swirl and pressurize the flow when blood is flowing through inducer and impeller. Therefore, varying these parameters could possibly increase the pressure as well as the hydraulic efficiency. In addition, there are four parameters demonstrating negative slope as shown from Figure 4.5 to Figure 4.7.

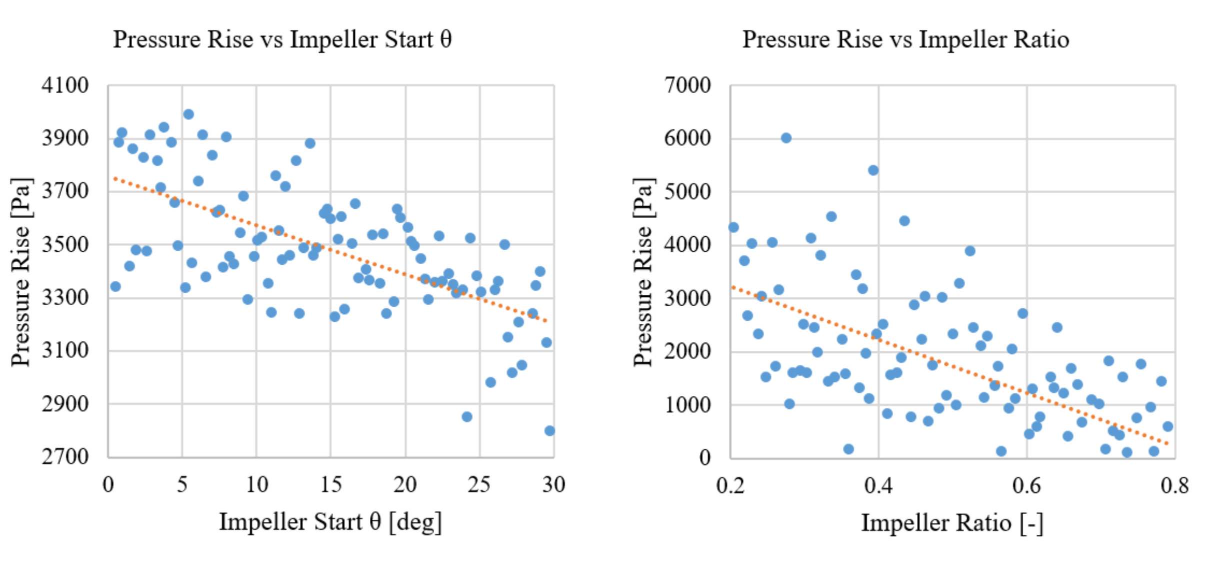

Figure 4.5: Pressure rise versus impeller start angle (left) and impeller ratio (right)

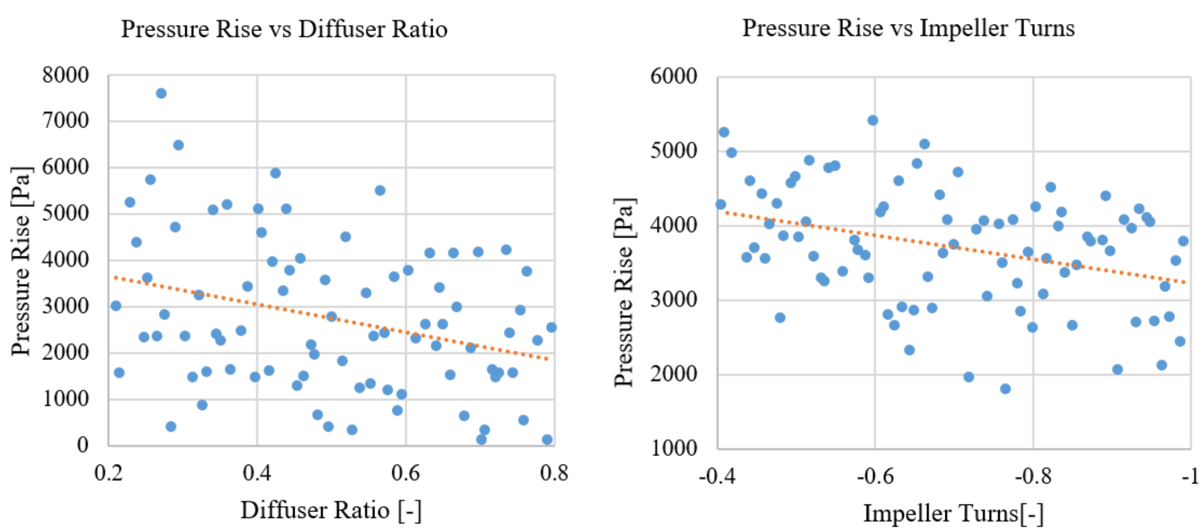

Figure 4.6: Pressure rise versus diffuser ratio (left) and impeller turns (right)

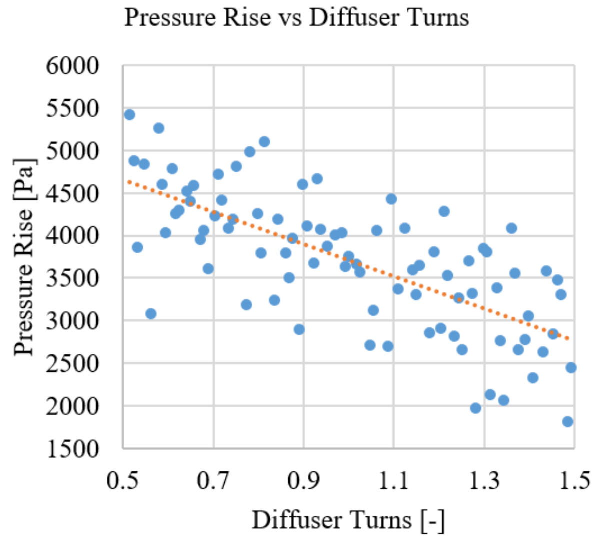

Figure 4.7: Pressure rise versus diffuser turns

The parameters with significant negative slope are also related to impeller and diffuser. By increasing the impeller and diffuser ratio, the impeller blades and the primary set of blades in diffuser would have a smaller blade width with respect to x and y direction. In other words, the blades will be closer to the outer shell and the size of secondary diffuser, the volute, will increase. Therefore, the flow in the center area could lose more pressure instead of recovering pressure by the primary blades. On the other hand, increasing the impeller and diffuser turns in a specific range could reduce the pressure rise due to larger surface area and longer path for the flow. However, it is believed that there should be an optimal point for both of the turns that can be explored by other optimization algorithms for future work. Within the limited range from 0.5 to 1.5 for diffuser turns and -0.4 to -1 for impeller turns, the general trend shows they have an inversely proportional relationship with pressure rise.

4.1.2 Hemolysis Index (HI)

There are four parameters proportional to HI including pump outer diameter, impeller start angle and number of blade and diffuser blade length as shown in Figure 4.8 and Figure 4.9.

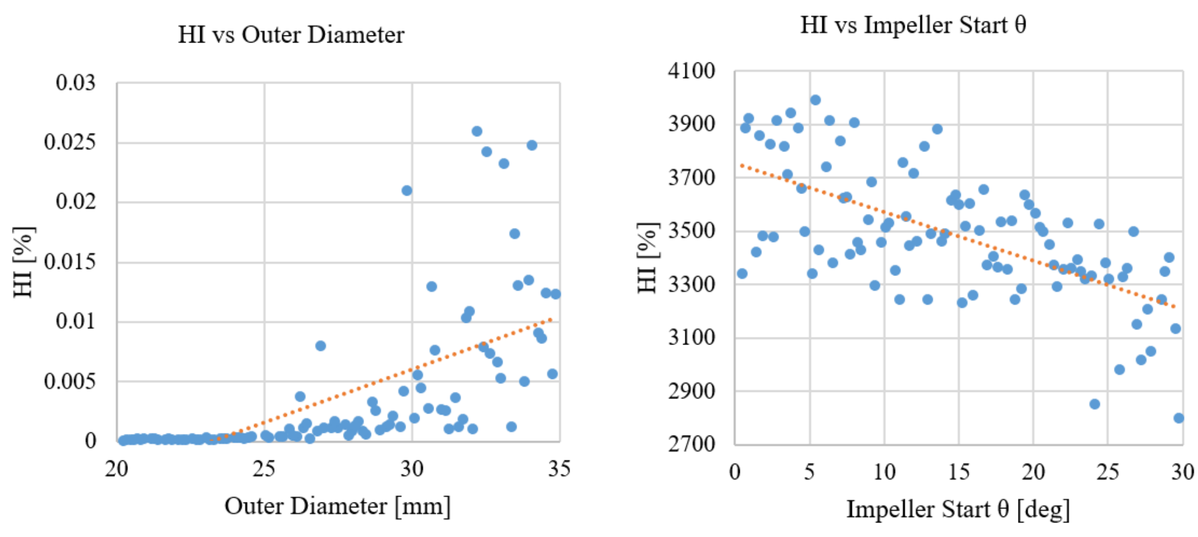

Figure 4.8: HI versus outer diameter (left) and impeller start angle (right)

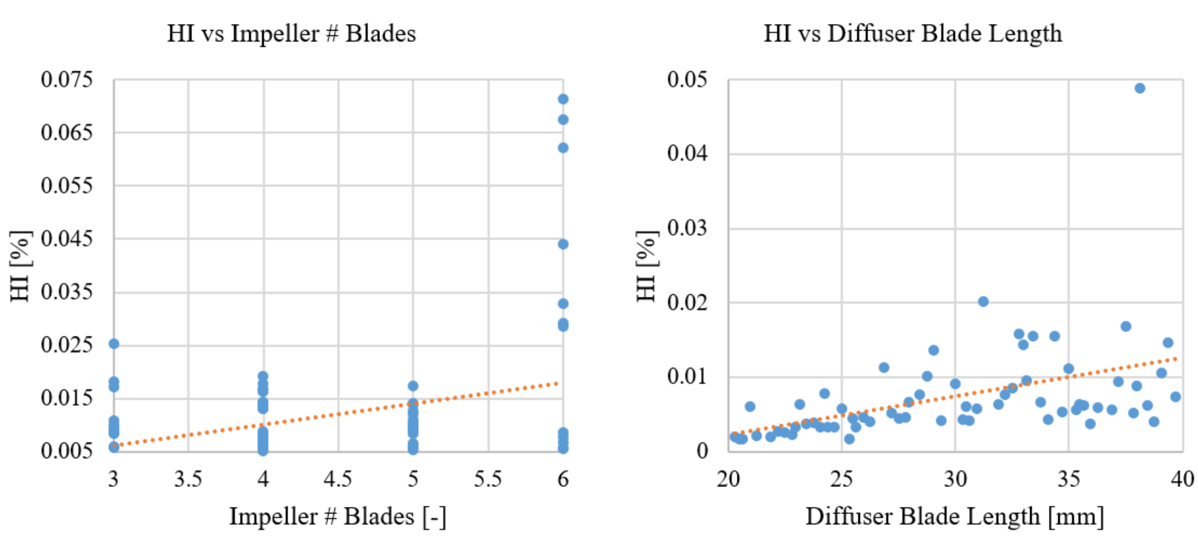

Figure 4.9: HI versus impeller number of blades (left) and diffuser blade length (right)

The parameters that could positively affect HI mainly come from the impeller and diffuser, similar to pressure rise. In addition, inducer number of blades also shows the proportional correlation to HI. One of the reasons HI is affected by inducer and impeller number of blades and parameter x is that it is positively related to the path length of a cell. The more the contact with the device, the higher the HI would be. Moreover, there are three parameters that have negative effect on HI, as shown in Figure 4.10.

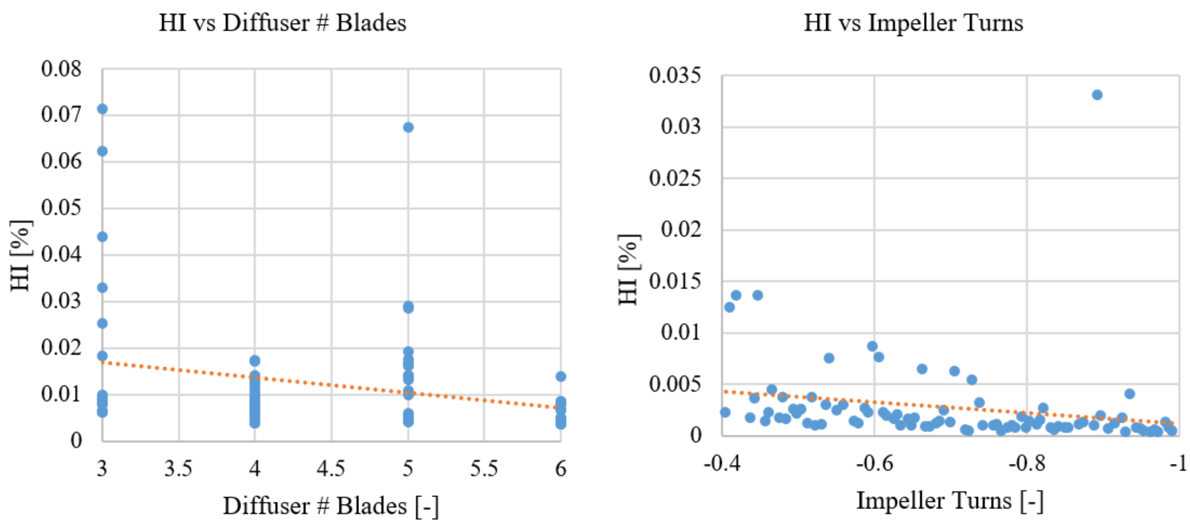

Figure 4.10: HI versus diffuser number of blades (left) and impeller turns (right)

Starting from impeller and diffuser turns, the larger the turn is, the smaller the outer blades are. Therefore, reducing the number of turns could possibly reduce the contact between blood cells and the device, and then result in reducing HI. However, different from the trend for inducer and impeller number of blades, diffuser number of blades shows an inversely proportional correlation to HI. In fact, there are two possible reasons causing this issue. Firstly, outliers that occurs at three blades geometry that could cause linear correlation to deviate. Secondly, there were 100 geometry variants for number of blades parameter group, and it may not be distributed to number of blades from three to six evenly. In this case, the number of runs with six blades geometry is less than the rest of number of blades. It might be another error source for generation of the linear regression.

4.1.3 Parameter Ranking

With respect to both of the evaluation parameters, pressure rise and HI, Least Squares Regression Method was used to quantify the sensitivity of all parameters. The value of correlations, or the slope of each parameter, was ranked and then normalized by dividing each term by the maximum value of the corresponding series in which outer diameter for both pressure sensitivity table and HI sensitivity table. The result is shown in Table 4.1 and Table 4.2.

Table 4.1: Normalized parameter sensitivity versus pressure rise

Parameters	**Normalized Sensitivity**
Outer diameter	1.000
Diffuser number of blades	0.936
Diffuser blade length	0.821
Impeller ratio	-0.546
Outlet diameter	0.465
Impeller blade length	0.465
Impeller number of blades	0.422
Diffuser turns	-0.403
Impeller turns	-0.257
Impeller parameter x	0.236
Inducer blade length	0.218
Secondary diffuser number of blades	0.154
Inducer number of blades	0.144
Secondary diffuser turns	0.141
Secondary ratio	-0.085
Impeller start angle	-0.084
Inducer gap	0.052
Impeller end angle	0.046
Inducer parameter x	0.040
Induce ratio	-0.037

Inducer turns	-0.036
Diffuser parameter x	-0.031
Secondary diffuser parameter x	0.031
Diffuser gap	0.020
Impeller gap inducer side	-0.018
Impeller gap diffuser side	-0.017
Inducer end angle	0.011
Diffuser end angle	-0.008
Diffuser start angle	0.004
Inducer start angle	-0.003
Secondary diffuser start angle	-0.001
Secondary diffuser end angle	0.001

Table 4.2: Normalized parameter sensitivity versus HI

Parameters	**Normalized Sensitivity**
Outer diameter	1.000
Impeller number of blades	0.686
Diffuser blade length	0.559
Diffuser number of blades	-0.515
Inducer number of blades	0.467
Impeller parameter x	0.211
Inducer blade length	-0.210
Diffuser turns	-0.205
Impeller turns	-0.173
Impeller ratio	-0.165
Secondary parameter x	0.161
Outlet diameter	0.134
Impeller start angle	0.116
Secondary diffuser number of blades	-0.112
Inducer turns	0.102
Diffuser parameter x	-0.096
Inducer gap	0.095
Inducer parameter x	-0.086
Secondary diffuser end angle	0.076
Secondary diffuser ratio	-0.069
Impeller gap inducer	0.064
Inducer start angle	-0.061
Impeller gap diffuser side	0.061
Secondary diffuser turns	-0.059
Diffuser gap	0.053

Diffuser end angle	-0.041
Secondary diffuser start angle	-0.041
Diffuser start angle	-0.039
Inducer ratio	0.034
Impeller end angle	-0.029
Impeller blade length	-0.023
Inducer end angle	0.017

Negative value in normalized sensitivity represents the parameters' inversely proportional correlations. Among these parameters, most of the sensitive parameters have same correlations, either positive or negative, with respect to both pressure rise and HI, including outer diameter, diffuser number of blades, blade length and turns as well as impeller parameter x, blade length and ratio. Therefore, necessary tradeoff must be made in order to optimize this model to maximize the pressure rise as well as minimize the HI. For example, impeller ratio is the fourth place in pressure rise table, but only 10^{th} place in HI table. Since the more sensitive evaluation will take the dominant position for impeller ratio, in this case, the pressure is the priority. Similarly, the sensitivity comparisons between versus pressure rise and versus HI have been performed for all parameters and the final optimized model has been generated.

4.2 Comparison between Baseline and Optimized Models

4.2.1 CFD Comparison

The velocity streamlines comparison between baseline and optimized model is shown in Figure 4.11 and Figure 4.12. Both models have 200 streamlines with the start position at inducer-impeller and impeller-diffuser interfaces.

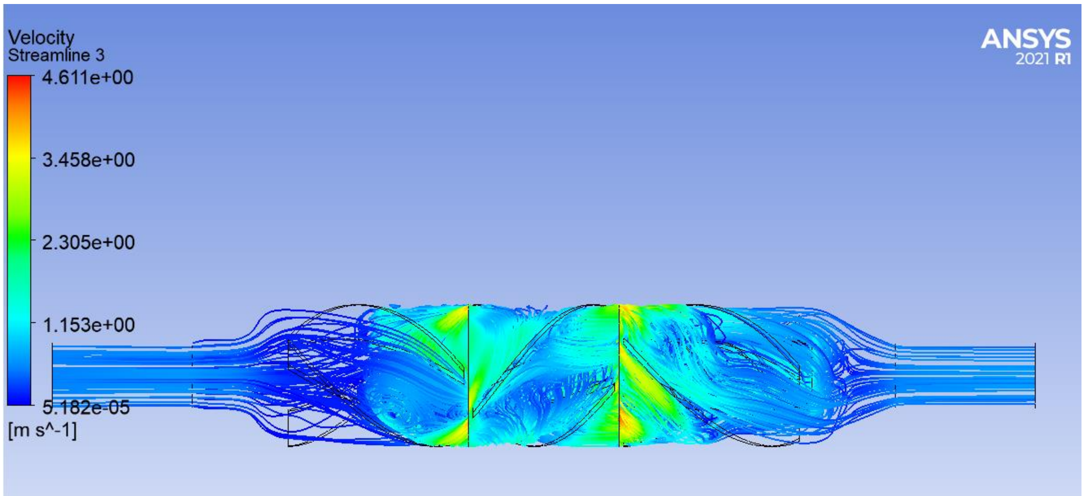

Figure 4.11: Velocity streamline for baseline model

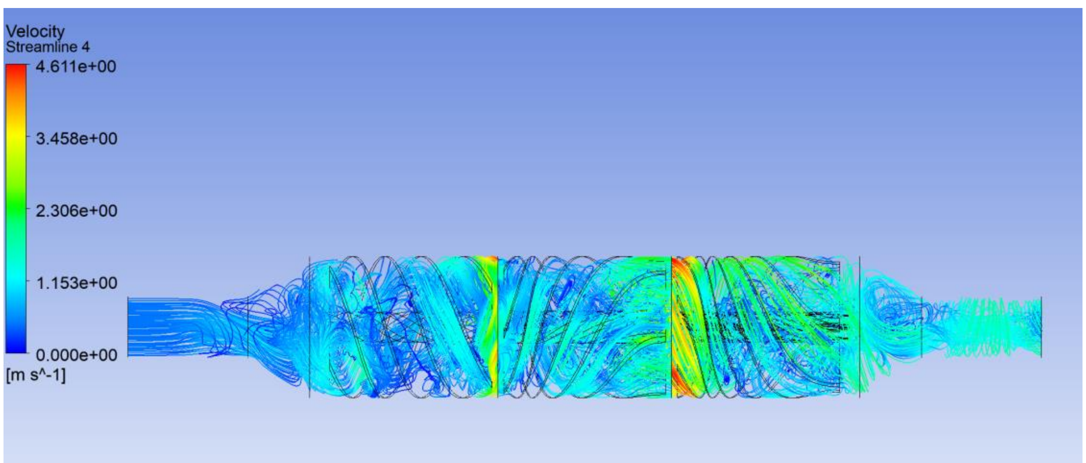

Figure 4.12: Velocity streamline for optimized model

The maximum velocity in optimized model is 5.33 [m s^{-1}] while it is 4.61 [m s^{-1}] in baseline model. The baseline model has more evenly distributed streamlines while the optimized model has the higher velocity concentrating at impeller-diffuser interface. One of the reasons is that optimized impeller blade curvature could provide higher pressure when fluid flowing through impeller. Then the flow passes the optimized diffuser blades resulting in more pressure recovered comparing to baseline model. Wall shear contour was also compared between baseline and optimized model as shown in Figure 4.13 and Figure 4.14. The maximum wall shear occurred at the end of impeller blade and the start position of diffuser blade for both of the model. The main reason for this is that the impeller is a rotating domain and the flow slowing down at the connection between impeller and diffuser could cause large wall shear.

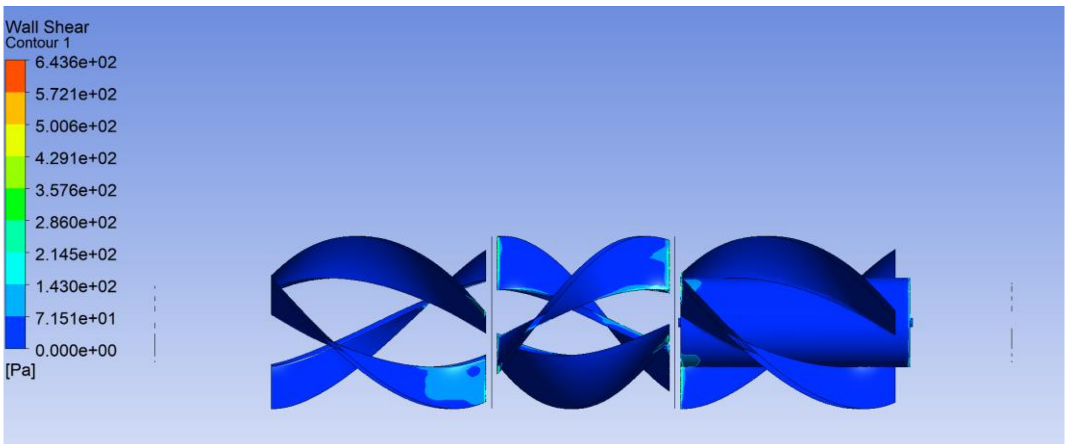

Figure 4.13: Wall shear contour at blades of baseline model

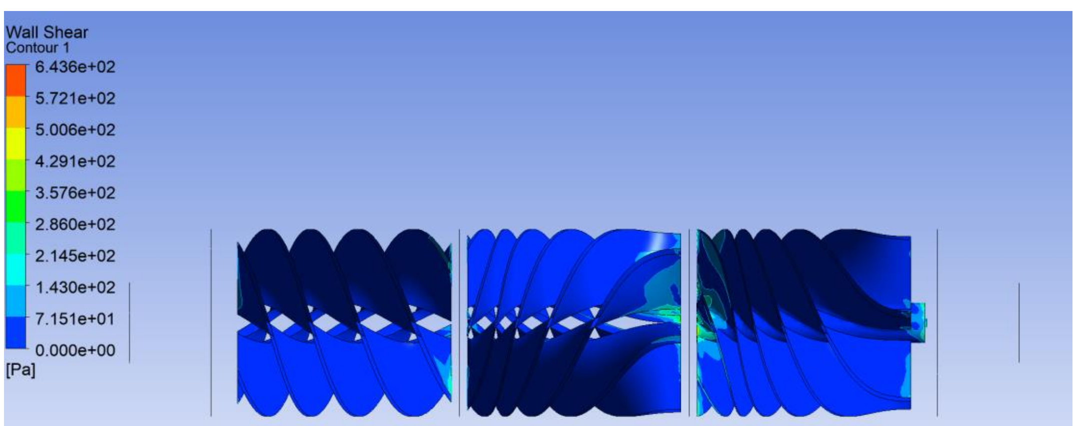

Figure 4.14: Wall shear contour at blades of optimized model

For the output evaluation parameters comparing the baseline model, the pressure increased from 2806 Pa to 14102 Pa, equivalent to 21.05 mmHg to 105.77 mmHg; HI increased from 0.0021 to 0.0024; hydraulic efficiency increased from 7.6 % to 59.6 %; average shear stress throughout the whole assembly increased from 19.9 Pa to 60.5 Pa; maximum shear stress also increased from 804 Pa to 1359 Pa. The comparison is shown in Table 4.3 below.

Table 4.3: Comparison of evaluation results between baseline and optimized model

Evaluation Results	Baseline Model	Optimized Model
Pressure [mmHg]	21.05	105.77
HI [%]	0.0021	0.0024
Efficiency [%]	7.6	59.6
Average Shear Stress [Pa]	19.9	60.5
Maximum Shear Stress [Pa]	804	1359

Comparing all evaluation parameters, it is acceptable to increase the pressure rise over 5 times as well as increase the hydraulic efficiency closed to an order of magnitude with only 12.5% increase for HI. As for average and maximum shear stress, they could be used as reference parameters since there are some uncertainties when calculating them. One of the major uncertainty sources is small y+ value when meshing the fluid domain. Generally, when y+ value is lower than 10, the shear stress at the walls could be possibly overestimated. Therefore, by comparing the primary parameters of pressure rise, HI and hydraulic efficiency, the optimized model is able to reach the expected systolic and diastolic pressure while roughly keep the HI the same value as the baseline model.

4.2.2 Parameters Comparison

In order to optimize the baseline geometry, the parameters that show clear trend versus pressure rise and HI are assigned with the optimal value within the range. The rest of parameters without strong correlations were assigned with values that was occurred in previous individual optima. Comparing to the baseline model, the following parameters have been changed to achieve better pressure rise and hydraulic efficiency showing in Comparison between baseline model and optimized model in Table 4.4 below.

Table 4.4: Comparison between baseline model and optimized model

Parts	Parameters	Baseline Value	Optimized Value	Units
Diffuser	Outer Diameter	30	35	[mm]
	Outlet/Inlet Diameter	14	15	[mm]
	Ratio	0.5	0.2	[-]
	Turns	0.4	0.89	[-]
	Parameter x	0.5	0.9	[-]
	Number of Blades	3	6	[-]
	Length	37	40	[mm]
	Start Angle	0	27	[Deg]
Secondary Diffuser	Turns	0.4	2	[-]
	Number of Blades	3	6	[-]
	Parameter x	0.5	0.9	[-]
Impeller	Ratio	0.5	0.21	[-]
	Turns	-0.4	-0.82	[-]
	Number of Blades	3	6	[-]
	Parameter x	0.5	0.94	[-]
	Length	30	40	[mm]
	End Angle	0	35	[Deg]
Inducer	Ratio	0.5	0.2	[-]
	Turns	0.4	1.06	[-]
	Parameter x	0.5	0.63	[-]
	Number of Blades	3	6	[-]
	Length	37	40	[mm]
	Start Angle	0	25	[Deg]
	End Angle	0	30	[Deg]

Most of the parameters were increased to achieve better pressure rise and hydraulic efficiency following the parameter sensitivity table shown in the previous section. For example, the number of blades of all parts was increased from three to six, and the blade length for all parts was increased from 30 mm and 37 mm to 40 mm. In addition, the start and end angles for each of the parts were also adjusted accordingly based on the simulation results and sensitivity analysis. On the contrary, three parameters were decreased including inducer ratio, impeller ratio and diffuser ratio. They were also consistent with previous section since the smaller the ratio was, the larger the blade (primary set of blades for diffuser) was. Then larger blades could help pressurizing flow as well as recovering the pressure. These parameter ranges were limited due to geometry generation failure if one or more parameters went closed to the boundary limit and it will be discussed in chapter 5 for further details.

Chapter 5: Limitations and Future Work

5.1 Limitations and Uncertainties

The optimized model in this thesis, compared to baseline model, has an improved pressure rise and hydraulic efficiency with a relatively small increase in hemolysis index and it validates the possibility of the novel configuration of the LVAD. However, there are several limitations that could possibly affect the accuracy of the results. First of all, the CFD results shown a convergence criterion of 10^{-3} instead of 10^{-4} mentioned in Chapter 3. One of the main reasons is that there was quasi-unsteady phenomena in CFD results that are difficult to capture with a RANS simulation. It was tested and able to reach 10^{-4} under the transient setting with 0.3 second for total time and 0.008333 second, calculated by time consumed for 10 resolutions under 2000 RPM rotational speed. In addition, under transient setting, the interface model could be selected as transient rotor-stator, in which there is no need to model the interface mechanics and the inherent unsteadiness of blades passing over the stators. However, solving one single transient simulation would take over 3 hours and it was too computationally expensive for over 500 geometry variants. Therefore, it is suggested to run further transient simulations optimization on more powerful server to improve efficiency while obtain accurate simulation results.

When evaluating hemolysis using index Giersiepen-Wurzinger equation, the coefficient used in calculation was $HI\,[\%] = 3.62 \times 10^{-5} \times \tau^{2.416} \times t^{0.785}$. However, for human blood, the constant in this equation depends on the shear rate in the environment and it was hard to model shear rate accurately within a LVAD since it varied node to node. Moreover, the Lagrangian approach to evaluating hemolysis index is inherently less accurate than the Eulerian method, due to the inherent difficulty of obtaining a uniform sample of data from the domain, and the inherent sensitivity of HI to streamline number and seeding locations. In addition, the blood was modeled as a Newtonian fluid under high shear rate while the red blood cells were not explicitly modeled which could possibly increase the validity of the hemolysis simulation.

Also, the Least Squares Regression method works only well for linear correlations when evaluating parameter sensitivity. Some of the parameters may have exponential or polynomial relationship with evaluation objectives (pressure, HI and efficiency), and such relationships may appear more uncorrelated when evaluated using linear regression.

For CFD results, some vortices were found within the impeller and diffuser blades. These vortices could possibly be further reduced by further optimizing the blade shapes to recover more pressure and eventually, achieving better hydraulic efficiency. Moreover, backflow was found at the end of the secondary diffuser, mainly because when decreasing the diffuser ratio, the flow in primary diffuser near the shroud side would have higher velocity comparing to the diffuser wall. Then there was a radial pressure gradient from outer wall to the shroud and cause backflow into the secondary diffuser. It could be reduced or eliminated by changing the length of the shroud and testing different combination of shroud length and diffuser ratio, which was not discussed in previous chapters as it was outside of the initial scope of this analysis.

Lastly, only around two thirds of all parameters have been tested due to time and computational constraints. For example, shroud thickness and blade thickness were set up but not tested yet mainly because they might not be as sensitive as the rest of the blade parameters. More importantly, the parameter groups were not perfectly set up since parameters were not entirely independent from parameters in other groups. For example, the range of start and end angles of each part was limited due to interfered angles by the turns, which could cause geometry generation failure. Therefore, the exploration of the range for each of the parameters was not fully completed and could be further optimized.

5.2 Future Work

As not all the parameters were tested, the rest of parameters can be grouped as one or more independent groups and tested for their sensitivity such as shroud thickness. These parameters may not be as sensitive as the blade parameters to the pressure rise but varying them would change the flow as well as affect the hemolysis index calculation. In addition, the five parameter groups may be in some way dependent since they could affect each other by limiting their range. If computing resources were not limited, more independent groups with less parameters in each group should be tested for more accurate correlations. Moving on, multi-objective optimization algorithms such as Non-dominated Sorting Genetic Algorithm (NSGA II) and multi-objective simulated-annealing algorithm (MOSA) that have a high tolerance to simulation output parameter noise, should be considered for further optimization with the consideration of more evaluation parameters such as average and maximum shear stress. Furthermore, more precise blood damage prediction methods are available and can be adapted including strain-based hemolysis modeling. Also, the generation of streamlines could also be improved by increasing interpolation points and the number of streamlines.

Finally, all the current design exploration results are based on the numerical solutions solved by ANSYS CFX. Further validation from experimental data obtained from the test rig is required to validate the current CFD results.

5.3 Conclusion

In this thesis, a CFD-based geometry optimization and design exploration for a novel configuration of LVAD was conducted with 48 parameters in 5 independent parameter groups. Over 500 geometry variants were analyzed and compared to achieve an optimized geometry configuration. Within all the design variables, outer diameter, diffuser ratio, diffuser number of blades, impeller ratio and impeller number of blades have been found to be the most sensitive parameters to both pressure rise and hemolysis index (HI). Comparing to baseline geometry, the optimized geometry has increased the pressure rise from 2804 Pa to 14102 Pa, equivalent to 21.05 mmHg to 105.77 mmHg, while also increased HI from 0.0021 to 0.0024. Although the HI should be minimized based on the objective of this thesis, it can be considered as a reasonable compromise for recovering pressure nearly five times than before while only increasing the HI by 15%. Consequently, the hydraulic efficiency has also been increased from 7.6% to 59.6%.

This study is the first optimization step in designing a novel configuration of LVAD and the CFD results have validated the potential possibilities of hubless design LVAD after optimization. With further adaptation of HI modeling methods with higher accuracy, multi-objective optimization algorithm and access to more powerful computing resources, the hubless design LVAD is believed to be a feasible and practical long-term treatment for heart failure patients.

References

1. Virani, S. S. *et al*. Heart Disease and Stroke Statistics—2020 update: A report from the American Heart Association. Circulation (2020). doi:10.1161/CIR.0000000000000757.
2. McCarthy, P. M. HeartMate implantable left ventricular assist device: Bridge to transplantation and future applications. Ann. Thorac. Surg. 59, (1995).
3. Chung, Y., Cecere, R., Mongrain, R. & Azar, T. a Novel Dual-Angle Blade, Coreless Ventricular Assist Device. Can. J. Cardiol. 32, S173 (2016).
4. Mongrain, R., Chung, Y. H., Azar, T. & Cecere, R. Development of a New Hubless Ventricular Assist Device. Proc. 7Th Int. Conf. Mech. Mater. Des. 1565–1568 (2017).
5. Qiao, N. Final Report Redesign of diffuser for a Left Ventricular Assist Device (LVAD). Page 10 (2019).
6. Lim, H. S., Howell, N. & Ranasinghe, A. The Physiology of Continuous-Flow Left Ventricular Assist Devices. *J. Card. Fail.* 23, 169–180 (2017).
7. Cotoia, A. Pulmonary Vein. Available at: https://biologydictionary.net/pulmonary-vein/ (2020). (Accessed: 4th July 2021)
8. Miranda, G. M. Structure and Function of the Heart. Available at: https://www.news-medical.net/health/Structure-and-Function-of-the-Heart.aspx. (2021). (Accessed: 4th July 2021)
9. Hall, J. E. and Hall, M. E. Guyton and hall textbook of medical physiology. Fourteenth edition. Philadelphia, PA: Elsevier. (2021).
10. Mitchell, J. R. & Wang, J. J. Expanding application of the Wiggers diagram to teach cardiovascular physiology. *Adv. Physiol. Educ.* 38, 170–175 (2015).

11. Siriwardena, M. & Fan, E. Descent into heart and lung failure. Mechanical Circulatory and Respiratory Support (Elsevier Inc., 2018). doi:10.1016/B978-0-12-810491-0.00001-1.
12. Centers for Disease Control and Prevention. Heart Failure. Available at: https://www.cdc.gov/heartdisease/heart_failure.htm. (2021). (Accessed: 4th July 2021)
13. Friedrich, E. B. & Böhm, M. Management of End Stage Heart Failure. *Heart* 93, 626–631 (2007).
14. Authors, S. C., Of, N. & At, A. II. *Anatomy and physiology*. Acta Oto-Laryngologica vol. 19 (1934).
15. U.S. Department of Health & Human Services. Organ Procurement and Transplantation Network. Available at: https://optn.transplant.hrsa.gov/data/view-data-reports/national-data/#. (2021). (Accessed: 4th July 2021)
16. Timms, D. A Review of Clinical Ventricular Assist Devices. *Med. Eng. Phys.* 33, 1041–1047 (2011).
17. Maher, T. R. *et al.* Heartmate Left Ventricular Assist Devices: A Multigeneration of Implanted Blood Pumps. *Artif. Organs* 25, 422–426 (2001).
18. Rose, E. A. *et al.* Long-Term Use of a Left Ventricular Assist Device. *N. Engl. J. Med.* 345, 1435–1443 (2001).
19. Drews, T. *et al.* The 'Berlin Heart' Assist Device. *Perfusion* 15, 387–396 (2000).
20. John, R. Current Axial-Flow Devices-the HeartMate II and Jarvik 2000 Left Ventricular Assist Devices. *Semin. Thorac. Cardiovasc. Surg.* 20, 264–272 (2008).
21. Burke, D. J. *et al.* The HeartMate II: Design and development of a fully sealed axial flow left ventricular assist system. *Artif. Organs* 25, 380–385 (2001).

22. Park, S. J., Kushwaha, S. S. & McGregor, C. G. A. State-of-the-art Implantable Cardiac Assist Device Therapy for Heart Failure: Bridge to Transplant and Destination Therapy. *Clin. Pharmacol. Ther.* 91, 94–100 (2012).

23. Pagani, F. D. Continuous-Flow Rotary Left Ventricular Assist Devices with '3rd Generation' Design. *Semin. Thorac. Cardiovasc. Surg.* 20, 255–263 (2008).

24. Mehra, M. R. *et al.* A Fully Magnetically Levitated Left Ventricular Assist Device — Final Report. *N. Engl. J. Med.* 380, 1618–1627 (2019).

25. Farrar, D. J. *et al.* Design Features, Developmental Status, and Experimental Results with The Heartmate III Centrifugal Left Ventricular Assist System with a Magnetically Levitated Rotor. *ASAIO J.* 53, 310–315 (2007).

26. Abbott Inc. HeartMate LVAD. Available at: https://www.heartmate.com/healthcare-provider/heartmate-3-lvad. (2021). (Accessed: 4th July 2021)

27. Arndt, A. *et al.* Physiological Control of a Rotary Blood Pump with Selectable Therapeutic Options: Control of Pulsatility Gradient. *Artif. Organs* 32, 761–771 (2008).

28. Schmid, C. *et al.* Influence of Inflow Cannula Length in Axial-flow Pumps on Neurologic Adverse Event Rate: Results From a Multi-center Analysis. *J. Hear. Lung Transplant.* 27, 253–260 (2008).

29. Research and Markets, "Ventricular Assist Device (VAD) Market - Global Industry Analysis, Size, Share, Trends and Forecast, 2014-2022," https://www.researchandmarkets.com/reports/4085063/ventricular-assist-device-vad-market-global. (2020). (Accessed: 4th July 2021)

30. Global Industry Analysts, “Global Left Ventricular Assist Device (LVAD) Industry,” https://www.reportlinker.com/p05957303/Global-Left-Ventricular-Assist-Device-LVAD-Industry.html?utm_source=GNW. (2021). (Accessed: 4th July 2021)

31. Grand View Research, “Ventricular Assist Device Market Size, Share & Trends Analysis Report By Product (LVAD, RVAD, BiVAD, TAH), By Type Of Flow (Pulsatile, Continuous), By Design, By Application, By Region, And Segment Forecasts, 2020 – 2027,” https://www.grandviewresearch.com/industry-analysis/ventricular-assist-devices-market. (2020). (Accessed: 4th July 2021)

32. Windmill Cardiovascular Systems Inc. TORVAD: Toroidal Ventricular Assist Device. Available at: http://www.windmillcvs.com/. (2018). (Accessed: 4th July 2021)

33. CorWave, CorWave LVAD: The Next Gen LVAD. Available at: https://www.corwave.com/product/corwave-lvad/. (2021).(Accessed: 4th July 2021)

34. Evaheart Inc. A Reliable Device That Can 'Live' with Heart Failure Patients. Available at: http://www.evaheart-usa.com/. (2021). (Accessed: 4th July 2021)

35. Waters, B. H., Smith, J. R. & Bonde, P. Innovative free-range resonant electrical energy delivery system (FREE-D System) for a ventricular assist device using wireless power. *ASAIO J.* 60, 31–37 (2014).

36. Waters, B. *et al.* Toward Total Implantability Using Free-Range Resonant Electrical Energy Delivery System: Achieving Untethered Ventricular Assist Device Operation Over Large Distances. *Cardiol. Clin.* 29, 609–625 (2011).

37. Pya, Y. *et al.* First Human Use of a Wireless Coplanar Energy Transfer Coupled with a Continuous Flow Left Ventricular Assist Device. *J. Hear. Lung Transplant.* 38, 339–343 (2019).

38. Farinas, M.-I.; Garon, A.; Lacasse, D.; N'dri, D. Asymptotically Consistent Numerical Approximation of Hemolysis. Journal of Biomechanical Engineering, 128, 688. (2006).

39. Errill, E., Rheology of blood, Physiological Reviews, 49 (4), pp. 863-888 (1969).

40. Yamaguchi H. Engineering Fluid Mechanics. Dordrecht: Springer Netherlands; (2008).

41. Wiegmann, L. *et al.* Blood Pump Design Variations and Their Influence on Hydraulic Performance and Indicators of Hemocompatibility. *Ann. Biomed. Eng.* 46, 417–428 (2018).

42. Wells, R. E. & Merrill, E. W. Shear rate dependence of the viscosity of whole blood and plasma. *Science (80-.).* 133, 763–764 (1961).

43. Brooks, D. E., Goodwin, J. W. & Seaman, G. V. Interactions among erythrocytes under shear. *J. Appl. Physiol.* 28, 172–177 (1970).

44. Evans, E. & Fung, Y. C. Improved Measurements of the Erythrocyte Geometry. *Microvasc. Res.* 4, 335–347 (1972).

45. Yu, H. *et al.* A Review of Hemolysis Prediction Models for Computational Fluid Dynamics. *Artif. Organs* 41, 603–621 (2017).

46. Oguz K. Baskurt, Max R. Hardeman, Michael W. Rampling, Meiselman, H. J. *Handbook of Hemorheology And Hemodynamics*. *Journal of Chemical Information and Modeling* vol. 53 (2007).

47. Morphological Abnormalities of Red Blood Cells. *The Art of Medicine.* Available at: https://theartofmed.wordpress.com/2015/09/05/morphological-abnormalities-of-red-blood-cells/. (2021). (Accessed: 4th July 2021)

48. Arora, D., Behr, M. & Pasquali, M. A Tensor-Based Measure for Estimating Blood Damage. *Artif. Organs* 28, 1002–1015 (2004).

49. Reasor, D. A., Clausen, J. R., Aidun, C. K. Coupling the Lattice-Boltzmann and Spectrin-Link Methods for the Direct Numerical Simulation of Cellular Blood Flow. International Journal for Numerical Methods in Fluids, 68, 767–781. (2012).

50. Facts About Blood and Blood Cells. *Memorial Sloan Kettering Cancer Center.* Available at: https://www.mskcc.org/cancer-care/patient-education/facts-about-blood-and-blood-cells. (2021). (Accessed: 4th July 2021)

51. Föller, M., Huber, S. M. & Lang, F. Erythrocyte programmed cell death. *IUBMB Life* 60, 661–668 (2008).

52. Qiang, Y., Liu, J. & Du, E. Dynamic fatigue measurement of human erythrocytes using dielectrophoresis. *Acta Biomater.* **57**, 352–362 (2017).

53. Musielak, M. Red blood cell-deformability measurement: Review of techniques. *Clin. Hemorheol. Microcirc.* 42, 47–64 (2009).

54. Olia, S. E. *et al.* Mechanical blood trauma in assisted circulation: Sublethal RBC damage preceding hemolysis. *Int. J. Artif. Organs* 39, 150–159 (2016).

55. Paul, R. *et al.* Shear Stress Related Blood Damage in Laminar Couette Flow. *Artif. Organs* 27, 517–529 (2003).

56. Giersiepen, M., Wurzinger, L. J., Opitz, R. & Reul, H. Estimation of Shear Stress-Related Blood Damage in Heart Valve Prostheses - In Vitro Comparison of 25 Aortic Valves. *Int. J. Artif. Organs* 13, 300–306 (1990).

57. Heuser G, Opitz R. A Couette viscometer for short time shearing of blood. Biorheology 1980;17:17–24.

58. Zhang, T. *et al.* Study of flow-induced hemolysis using novel couette-type blood-shearing devices. *Artif. Organs* 35, 1180–1186 (2011).

59. Chung, T. J. *Computational fluid dynamics, second edition*. *Computational Fluid Dynamics, Second Edition* vol. 9780521769693 (2010).

60. Anderson, J. D. Governing Equations of Fluid Dynamics. *Comput. Fluid Dyn.* 15–51 (1992) doi:10.1007/978-3-662-11350-9_2.

61. Navier-Stokes equations. online.com Available at: https://www.cfd-online.com/Wiki/Navier-Stokes_equations. (Accessed: 4th July 2021)

62. Ansys® Help Viewer, Release 21R1, Help System, CFX User's Guide, ANSYS, Inc. (2021).

63. White, F., *Fluid mechanics*, McGraw-Hill, New York, US. (2008).

64. Mahalingam, A. *et al.* Numerical analysis of the effect of turbulence transition on the hemodynamic parameters in human coronary arteries. *Cardiovasc. Diagn. Ther.* 6, 208–220 (2016).

65. Indhumathi Devi, D., Chithra, S. & Sethumadhavan, M. Hardware random number generator using FPGA. *J. Cyber Secur. Mobil.* 8, 409–418 (2019).

66. Yalçin, M. E., Suykens, J. A. K. & Vandewalle, J. True random bit generation from a double-scroll attractor. *IEEE Trans. Circuits Syst. I Regul. Pap.* 51, 1395–1404 (2004).

67. Burhenne, S., Jacob, D. & Henze, G. P. Sampling Based on Sobol Sequences For Monte Carlo Techniques Applied To Building Simulations Fraunhofer Institute for Solar Energy Systems , Freiburg , Germany University of Colorado , Boulder , USA Corresponding author . E-mail address : sebastian.burhen. *Proc. Build. Simul. 2011 12th Conf. Int. Build. Perform. Simul. Assoc.* 14–16 (2011).

68. Savine, A., *Modern Computational Finance.* P. 205 (1970)

69. CAESES Documentation, Release 5.0.5, FSobol, Friendship System. (2021).

70. Cimrák, I., Gusenbauer, M. & Schrefl, T. Modelling and Simulation of Processes in Microfluidic Devices for Biomedical Applications. *Comput. Math. with Appl.* 64, 278–288 (2012).

Appendix A. Evaluation Standards for Mesh Quality

There are several indicators for evaluating mesh quality including skewness, orthogonal quality and aspect ratio. Skewness determines the difference between the shape of a cell and the shape of equilateral cell of same volume. The desirable value of skewness is 0 while high skewness closed to 1 will reduce the accuracy and reliability of the simulation results. Orthogonal quality measures the angular differences between the normal vector on the face of a cell and the normal vector from node to node of the same cell. The desirable value of orthogonal quality is 1 while value closed to 0 shows a poor quality in mesh. In addition, aspect ratio measures the deviation of an element from having an equilateral shape for all sides. Generally, the aspect ratio below 100 is desirable. Table A1 below shows the skewness and orthogonal quality mesh metrics spectrum.

Table A1: Skewness and orthogonal quality mesh metrics spectrum

Mesh Quality	Excellent	Very Good	Good	Acceptable	Bad	Unacceptable
Skewness	0-0.25	0.25-0.5	0.5-0.8	0.8-0.94	0.95-0.97	0.98-1.00
Orthogonal Quality	0.95-1.00	0.70-0.95	0.20-0.69	0.15-0.20	0.01-0.14	0-0.01

Appendix B. ANSYS-CAESES Connection

Since the fluid domain was built and parametrized in CAESES, it was exported as a SAT file into destination folder that can be read by ANSYS Workbench. Then ANSYS SpaceClaim was used to open the geometry file and generate the name selections for further boundary conditions set up. Surfaces and boundaries were grouped together in CAESES and assigned a unique color ID by ARGB value, for surfaces that correspond to differing boundary conditions. Then in ANSYS SpaceClaim, the name selections were generated in a repeatable and automated manner by associating preset color ID output from CAESES in the SAT format. Python scripts were also used to automate the ANSYS mechanical meshing procedure of setting mesh size and number of inflation layers, as well as the solution processing with preset boundary conditions and retrieval of the 5 output parameters. The block diagram connection for geometry input, meshing, and CFD simulations in ANSYS Workbench is shown in Figure B1.

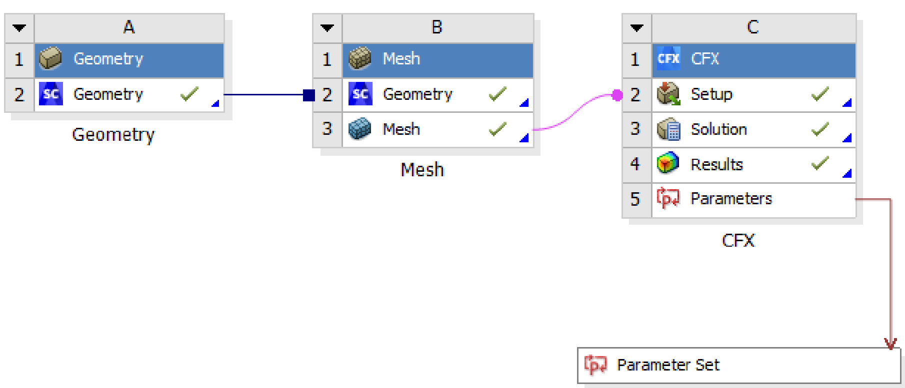

Figure B1: ANSYS block diagram showing Mesh and CFX connection

After obtaining CFD simulation results, ANSYS CFX would export five evaluation parameters as a *.csv* file in a preset directory by running ANSYS Workbench script. Then CAESES could read these parameters and generate the correlations between design variables (updated geometry parameter values) and evaluation parameters. The interface of the software connector in CAESES is shown in Figure B2. In CAESES, each optimization process would create a new folder. Therefore, in software connector, the directory of reading results and running Workbench in batch mode can be defined as variables in order to obtain the correct file location.

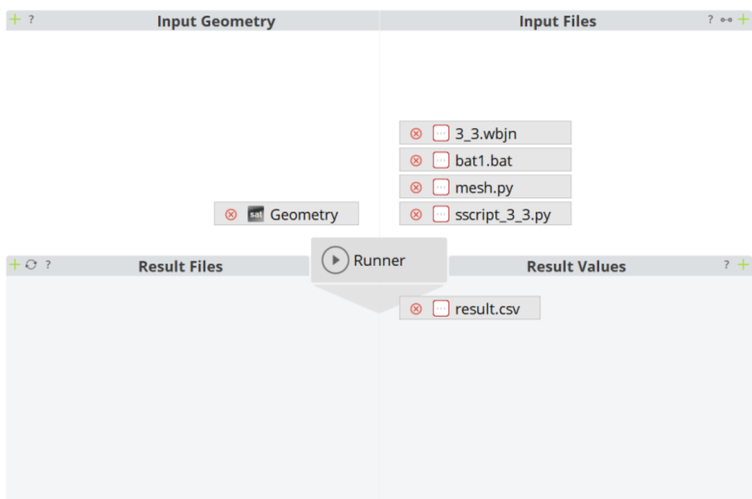

Figure B2: Interface of software connector in CAESES

From the top left, the input geometry is the SAT file generated by CAESES each time after updating the design variables. It will create a new optimization folder and export the SAT file into the specific directory. Then the input files from top right are: ANSYS Workbench journal file to trigger SpaceClaim and Mesh scripts as well as update and output the CFD results, Workbench batch file to run Workbench in batch mode, mesh script to set meshing settings, and SpaceClaim script to set name selections. Next, the result values from the bottom right are the *.csv* file exported by ANSYS CFX. CAESES is able to read the value from the file with pre-set row and column number and name it with corresponding parameter name. Moreover, the result file from the bottom left block can be the simulation files from various solvers such as *.cfx* and *.res* files generated by ANSYS CFX and then CAESES can save these files into the destination directory for future use. However, it does not affect the design exploration process and it was not used in this project.

In conclusion, the input geometry is generated and updated in CAESES each time varying the design variables. Then the geometry is meshed and simulated in ANSYS Workbench by Mesh Tool and CFX. Lastly, the results of 5 evaluation parameters are exported into CAESES and the loop is set up. Therefore, CAESES can create direct comparison and correlations between design variables (blade angle, turns, etc.…) and evaluation parameters (pressure rise, HI, etc.…).

Appendix C. Parameter Ranges for Design Exploration Study

Table C1: Detailed parameter ranges for design exploration study

Parts	Parameters	Baseline Value	Lower Limit	Upper Limit	Units
Diffuser	Outer Diameter	30	20	35	[mm]
	Outlet/Inlet Diameter	14	10	15	[mm]
	Ratio	0.5	0.2	0.8	[-]
	Turns	0.4	0.2	1.2	[-]
	Parameter x	0.5	0.1	0.9	[-]
	Number of Blades	3	3	6	[-]
	Length	37	20	40	[mm]
	Start Angle	0	0	35	[Deg]
	End Angle	0	0	30	[Deg]
Secondary Diffuser	Turns	0.8	0.8	2	[-]
	Number of Blades	3	3	6	[-]
	Parameter x	0.5	0.1	0.9	[-]
	Start Angle	0	0	30	[Deg]
	End Angle	0	0	30	[Deg]
Impeller	Ratio	0.5	0.2	0.8	[-]
	Turns	-0.4	-1	-0.4	[-]
	Number of Blades	3	3	6	[-]
	Parameter x	0.5	0.1	0.95	[-]
	Length	30	20	40	[mm]
	Start Angle	0	0	30	[Deg]
	End Angle	0	0	35	[Deg]
Inducer	Ratio	0.5	0.2	0.8	[-]
	Turns	0.4	0.4	1.06	[-]
	Parameter x	0.5	0.1	0.8	[-]
	Number of Blades	3	3	6	[-]
	Length	37	20	40	[mm]
	Start Angle	0	0	25	[Deg]
	End Angle	0	0	30	[Deg]

Appendix D. ANSYS Workbench Journal Script

ANSYS Workbench journal file was used to run SpaceClaim and Mesh script file within the workbench in order to set up name selections in SpaceClaim, mesh setting in ANSYS Mesh tool and boundary conditions in CFX solver. The script is shown below.

```
# encoding: utf-8
# 2021 R1
SetScriptVersion(Version="21.1.216")
print("Opening 3_3.wbpj...")
Open(FilePath="C:/Users/byn20/OneDrive/Desktop/Connector_3_3.wbpj")
print("Opening Geometry")
system1 = GetSystem(Name="Geom 1")
geometry1 = system1.GetContainer(ComponentName="Geometry")
geometry1.SetFile(FilePath="C:/Users/byn20/OneDrive/Desktop/mesh sensitivity_5_6.sat")
geometry1.Edit(IsSpaceClaimGeometry=True)
print("Running SpaceClaim Script...")
DSscript = open("C:/Users/byn20/OneDrive/Desktop/sscript_3_3 no blades.py", "r")
DSscriptcommand=DSscript.read()
DSscript.close()
geometry1.SendCommand(Command=DSscriptcommand, Language='Python')
Save(Overwrite=True)
geometry1.Exit()
#print("Updating Solution...")
```

```
#Update()
#print("Running SpaceClaim Script...")
system2 = GetSystem(Name="SYS 1")
mesh1 = system2.GetContainer(ComponentName="Mesh")
MSscript = open("C:/Users/byn20/OneDrive/Desktop/mesh.py", "r")
MSscriptcommand=MSscript.read()
MSscript.close()
mesh1.SendCommand(Command=MSscriptcommand,Language='Python')
Save(Overwrite=True)
mesh1.Exit()
meshComponent1 = system2.GetComponent(Name="Mesh")
meshComponent1.Update(AllDependencies=True)
print("Saving...")
Save(Overwrite=True)
print("Exporting .csv...")
Parameters.ExportAllDesignPointsData(FilePath="C:/Users/byn20/OneDrive/Desktop/result
.csv")
print("Export Done...")
```

Appendix E. ANSYS SpaceClaim Script

SpaceClaim script was used to set up name selections from previously assigned unique color ID from CAESES in order to assign correct surfaces and body in CFX for boundary conditions. The script is shown below.

```
# Python Script, API Version = V18
Face_colors = [[255, 175, 143, 143],
[255, 143, 175, 148],
[255, 175, 143, 172],
[255, 143, 174, 175],
[255, 143, 175, 146],
[255, 175, 143, 175],
[255, 165, 175, 143],
[255, 171, 175, 143],
[255, 143, 152, 175],
[255, 143, 149, 175]];
Face_Names = ["Diffuser_wall",
              "Impeller_wall",
              "Inducer_wall",
              "Inlet",
              "Outlet",
              "Ind_out",
              "Imp_in",
```

```
                    "Imp_out",
                    "Diff_in",
                    "Sec_blade"]
# Create Named Selection Group


for c,name in zip(Face_colors, Face_Names):
   refColor = Color.FromArgb(*c)
   primarySelection = PowerSelection.Faces.ByColor(refColor, PowerSelectOptions(True))
   secondarySelection =
PowerSelection.Faces.ByColor(refColor,PowerSelectOptions(True))
   result = NamedSelection.Create(primarySelection, secondarySelection)
   result = NamedSelection.Rename("Group1", name)
# EndBlock
Body_colors = [[255, 170, 143, 175],
[255, 175, 143, 143],
[255, 175, 155, 143],];
Body_Names = ["Diffuser",
                    "Impeller",
                    "Inducer"]
# Create Named Selection Group
for b,name in zip(Body_colors,Body_Names):
   refColor1 = Color.FromArgb(*b)
```

```
        primarySelection =
PowerSelection.Bodies.ByColor(refColor1,PowerSelectOptions(True))
        secondarySelection = PowerSelection.Bodies.ByColor(refColor1,
PowerSelectOptions(True))
        result = NamedSelection.Create(primarySelection, secondarySelection)
        result = NamedSelection.Rename("Group1", name)
    # EndBlock
```

Appendix F. ANSYS Mesh Script

ANSYS mesh script was used to set up mesh element size and number of inflation layers. The script is shown below.

```
'''NOTE : All workflows will not be recorded, as recording is under development.'''
#region UI Action
mesh_1 = Model.Mesh
mesh_1.ElementSize = Quantity(0.001, "m")
#endregion

#region UI Action
mesh_1 = Model.Mesh
mesh_1.UseAutomaticInflation = 1
#endregion
'''NOTE : All workflows will not be recorded, as recording is under development.'''
#region UI Action
mesh_1 = Model.Mesh
mesh_1.MaximumLayers = 4
#endregion
```

Appendix G. ANSYS Workbench Batch File Script

ANSYS workbench batch file was used to run workbench in batch mode and automate the optimization process. It was saved as *.bat* file and the script is shown below.

```
@echo off
del "C:\Users\byn20\OneDrive\Desktop\Connector_3_3_files\.lock"
@echo Ansys
call "C:\Program Files\ANSYS Inc\v211\Framework\bin\Win64\RunWB2.exe" -R "C:\Users\byn20\OneDrive\Desktop\Connector_3_3_14_5_8\81_diff_without_sec\diff_without_sec_81_des0001\Runner\3_3.wbjn "
```